White Rose Research Online

eprints@whiterose.ac.uk
https://eprints.whiterose.ac.uk
Universities of Leeds, Sheffield and York

Deposited via The University of Sheffield.

White Rose Research Online URL for this paper:
https://eprints.whiterose.ac.uk/id/eprint/246938/

Version: Published Version

Article:
Vigor, J.E., Friskney, A.A., Gilbert, R.R. et al. (2026) Solid-state and precipitation-based synthesis routes for zirconolite-rich powders for plutonium immobilisation. Journal of Nuclear Materials, 634. 157115. ISSN: 0022-3115

https://doi.org/10.1016/j.jnucmat.2026.157115

Reuse
This article is distributed under the terms of the Creative Commons Attribution-NonCommercial-NoDerivs (CC BY-NC-ND) licence. This licence only allows you to download this work and share it with others as long as you credit the authors, but you can't change the article in any way or use it commercially. More information and the full terms of the licence here: https://creativecommons.org/licenses/

Takedown
If you consider content in White Rose Research Online to be in breach of UK law, please notify us by emailing eprints@whiterose.ac.uk including the URL of the record and the reason for the withdrawal request.

UNIVERSITY OF LEEDS
University of Sheffield
UNIVERSITY of York

Journal of Nuclear Materials 634 (2026) 157115

Contents lists available at ScienceDirect

Journal of Nuclear Materials

journal homepage: www.elsevier.com/locate/jnucmat

Solid-state and precipitation-based synthesis routes for zirconolite-rich powders for plutonium immobilisation

James E Vigor [a,*], Aidan A Friskney [b], Reuben R Gilbert [a], Lewis R Blackburn [b], Katie Hadley [c], Paul Gilchrist [a], Richard White [c], Jason Farrell [a]

[a] Eden Nuclear and Environment Ltd., Unit 1 Mereside, Greenbank Road, Eden Business Park, Penrith, Cumbria, CA11 9FB, UK
[b] Immobilisation Science Laboratory, School of Chemical, Materials and Biological Engineering, University of Sheffield, S1 3JD, UK
[c] Lucideon Ltd., Stone Business Park, Brooms Road, Stone, Staffordshire, ST15 0SH, UK

HIGHLIGHTS

- Single zirconolite precursors simplify future Pu by rationalising input materials.
- Wet and dry routes both yield high-quality zirconolite for PuO_2 immobilisation.
- Ce-doped zirconolite consistently crystallises as mixed 2M/3T polytype assemblages.
- Fragment-morphology dry powders show superior flowability over finer wet powders.
- Precursor synthesis route influences powder processing and phase evolution.

ARTICLE INFO

Keywords:
Plutonium
Zirconolite
Immobilisation
Surrogates
Optimisation
Alkoxide

ABSTRACT

Zirconolite (prototypically $CaZrTi_2O_7$) is a wasteform system under consideration for the immobilisation of the United Kingdom's civil inventory of separated PuO_2. The laboratory-scale synthesis route for zirconolite typically adopted is a route whereby individual oxide precursor powders are co-milled with PuO_2 (or a non-radioactive surrogate such as CeO_2). However, translating this sort of approach to an industrial-scale process is likely to be challenging due to the difficulty of feeding multiple feedstocks into a Pu-active plant under stringent constraints. As such, a process route through which a single precursor could be prepared in a separate, upstream inactive facility, prior to being later combined with PuO_2, would be strategically advantageous. In this work, 'single zirconolite-rich precursor' approaches were investigated for synthesis of Ce-doped zirconolite, with both dry solid-state and wet alkoxide-nitrate precipitation synthesis routes utilised. These approaches were assessed using cold press and sinter trials in this case, with both dry and wet routes found to be capable of producing high density zirconolites. The dry route formed crystalline Ce-bearing zirconolite ceramics containing a relatively minor perovskite secondary phase. The wet-route precursor was significantly structurally disordered and subsequently formed a zirconolite-rich ceramic which also contained a perovskite secondary phase. Based on a limited study under consistent analytical conditions, it was also found that dry route reported a more predictable powder flow behaviour and therefore may offer a better route to future industrialisation. Overall, these results indicate that a single zirconolite-rich precursor may be a credible approach for wasteform synthesis in the context of PuO_2 immobilisation.

1. Introduction

The United Kingdom (UK) has a civil inventory of approximately 140 t. of separated plutonium, primarily in the form of PuO_2 powder; this material is stored in purpose-built packages and facilities at the Sellafield nuclear site which is owned by the UK Nuclear Decommissioning Authority (NDA), and operated by the NDA Group company Sellafield Ltd. Pu is highly radioactive and fissile, requiring specialised handling skills and facilities; stringent safety and security arrangements are required to store and account for plutonium. The UK Government's

* Corresponding author.
E-mail address: james.vigor@eden-ne.co.uk (J.E. Vigor).

https://doi.org/10.1016/j.jnucmat.2026.157115
Received 26 June 2026; Received in revised form 3 September 2026; Accepted 29 September 2026
Available online 30 September 2026
0022-3115/© 2026 The Authors. Published by Elsevier B.V. This is an open access article under the CC BY-NC-ND license (http://creativecommons.org/licenses/by-nc-nd/4.0/).

objective is to put the civil Pu inventory beyond reach, into a form which reduces the long-term safety and security burden during storage and ensures it is suitable for disposal in a Geological Disposal Facility (GDF). This will reduce long-term security risks and proliferation sensitivities for future generations. Following many years of evaluating technical and economic factors, in 2025 the UK Government announced a revised management strategy for UK civil Pu: to immobilise the PuO_2 in a stable wasteform, followed by permanent isolation in a future UK GDF.

To confer long-term and passive safety, the wasteform in which PuO_2 is immobilised must exhibit chemical, physical, and thermodynamic stability that can be reliably demonstrated over geological timescales. This has previously led to the identification of zirconolite ($CaZrTi_2O_7$), which exhibits a very low leach-rates for constituent cations [1,2] and high irradiation tolerance [3], as a viable candidate host phase [4]. Zirconolite ceramics (or oxide blends that can readily yield zirconolite by heating either as pellets or powders) have been produced by a variety of methods, including solid-state synthesis [5], combustion synthesis [6], and precipitation routes [7]. Typically, the most widely adopted route to produce zirconolite precursor blends involves the planetary co-milling of constituent oxide powders together with polar solvents such as isopropanol (IPA) or acetone. This can reduce agglomeration of powders, ease energy transfer to improve size reduction and are easily removed by evaporation.

The constituent precursor materials for zirconolite for Pu immobilisation are often $CaTiO_3$ (or potentially alternative Ca compounds such as $CaZrO_3$, CaO, or $CaCO_3$), ZrO_2 and TiO_2 as the key zirconolite formers, alongside Al_2O_3/Fe_2O_3 for formal charge balance, HfO_2 and/or Gd_2O_3 as neutron absorbers, and the PuO_2 (or a surrogate such as CeO_2 or ThO_2) to meet an appropriate target stoichiometry. The current 'baseline' composition being assumed for UK Pu immobilisation, and with Ce as a non-radioactive Pu surrogate, is $(Ca_{0.785}Ce_{0.2}Gd_{0.015})(Zr_{0.785}Ce_{0.1}Gd_{0.015}Hf_{0.1})(Ti_{1.6}Fe_{0.4})O_7$ at 95 wt.%, plus a 5 wt.% 'buffer' phase comprising $(Ti_{0.9}Hf_{0.1})O_2$; the intention of the buffer here is to provide an excess of Ti and, therefore, mediate the formation of undesirable secondary (or 'accessory') phases, in particular perovskite. In respect of this composition, the component oxide powders (often dried by heating in air before use) are typically homogenised and size reduced (in a co-milling process), pressed into pellets, and then sintered in a controlled atmosphere (cold press and sinter; CPS). Alternatively, the co-milled feed powder can be fed into a process such as hot isostatic pressing (HIP) which is the synthesis approach being assumed by the NDA for future 'industrial-scale' Pu immobilisation using a zirconolite. In a laboratory setting, synthesis by CPS is frequently used to produce zirconolites due to the practicality of using the method which provides an efficient synthesis route where a large number of samples are needed [8].

In practice, it could be challenging to translate the use of multiple feedstock powders as detailed previously into a plutonium-active industrial-scale process. Planetary milling could be difficult to scale beyond hundreds of grams powder mass, while the use of solvents such as acetone or IPA in a Pu-active context presents risks of combustion or nuclear criticality due to the neutron-moderating properties of these liquids. Moreover, working with six different feedstock powders (i.e., separate Ca, Zr, Ti, Fe, Hf and Gd oxides) with varying properties is likely excessively complex, particularly in a nuclear facility that has extensive design and operational constraints in place. Therefore, it could be advantageous if these six powders could instead somehow be 'pre-fabricated' into some form of *single* zirconolite-rich powder feedstock in a separate, upstream *non-nuclear* plant. This arising powder, which is referred to here as a 'single zirconolite-rich precursor', could then be imported into the Pu-active plant for further processing.

To our knowledge, the performance of a single zirconolite-rich precursor, in terms of powder properties, as well as the influence on the downstream sintered zirconolite ceramic, has not yet been compared with the aforementioned 'conventional' approach of co-milling of multiple (six) powders. This presents a substantial gap which must be addressed before a decision (by the NDA) can be made on which approach to pursue for future industrial-scale research and development. Moreover, if a single zirconolite-rich precursor was to be adopted, there is interest in how the powder synthesis route might be optimised – with both solid-state ('dry') and liquid chemical ('wet') powder synthesis routes potentially viable. As such, the aim of the work reported here is to investigate single zirconolite-rich precursor materials produced using these dry and wet synthesis approaches, and to evaluate how the respective processing routes influence precursor characteristics and subsequent wasteform formation.

2. Materials and characterisation methods: general

The single zirconolite-rich precursor wet route and dry route experimental activities were carried out in two different research establishments, the University of Sheffield and Lucideon Ltd. Therefore, due to different experimental facilities between these two organisations, as well as some constraints associated with materials availability, the comparison between the wet and dry route activities reported in this work is not entirely on a 'like for like' basis, and limitations in interpretation which arise as a result of this are covered extensively in Section 2.1.

The analytical methods available for characterisation of powder samples were particle size distribution (PSD), specific surface area (SSA), thermogravimetric analysis (TGA), morphology and chemical homogeneity using scanning electron microscopy (SEM) with energy-dispersive X-ray spectroscopy (EDS), and a powder rheometry approach using a Malvern Panalytical Freeman FT4 powder rheometer (referred to as FT4). Sintered pellet samples have been characterised for density, phase composition (using a pulverised sample) with powder X-ray diffraction (XRD; Cu-Kα) and Rietveld crystal structure refinement, and chemical homogeneity using SEM-EDS. To maintain confidence in the assessment, no direct comparison was made between results where analytical techniques sufficiently diverged.

Differences in the availability of analytical equipment between the two institutions meant that some data were acquired under differing conditions. To make these differences explicit, Table 1 summarises the principal characterisation methods used and instrument settings, relevant to the interpretation of results here.

2.1. Analytical limitations

The use of different instrumentation introduces varying levels of uncertainty into comparisons between the wet and dry route data and makes it challenging to confidently draw direct comparisons between these groups. In this case, PSD, SSA, and FT4 data were collected using equivalent instrumentation and methods. However, this was not the case for TGA, SEM-EDS, and XRD measurements, and a greater degree of caution is required in interpretation of these data.

TGA measurements were acquired using different instruments and different sample masses, and this may affect thermodynamics, mass transfer rates, and off-gas evolution. Therefore, the apparent onset, duration, rate, and magnitude of individual decomposition events may be reported inconsistently between the two instruments. In this paper, TGA was therefore only used to identify the presence and approximate range of decomposition events with broad approximation of mass-loss and no specific peak integration. No strict quantitative like-for-like comparison of samples is presented here, and statistics from these data, if reported, are given independently for each material.

Comparisons between samples based on SEM-EDS analysis will have been affected by the differing spatial resolution of the FEG-SEM and benchtop SEM systems, and it is likely that fine scale segregation will have remained unresolved in the wet-route material. However, SEM-EDS was used here primarily to assess elemental distributions, alongside some secondary spot analysis for verification of composition using the higher resolution SEM-EDS instrument. The data were used here to

Table 1
Summary of the principal analytical methods used for the dry and wet route materials and differences relevant to the comparison of the resulting datasets.

Instrument	Dry Route	Wet Route	Principal Difference
PSD	Malvern Panalytical Mastersizer 3000 PSA	Malvern Panalytical Mastersizer 3000 PSA	Equivalent.
SSA	Micromeritics TriStar II Plus N_2 at 77 K	Micromeritics TriStar II Plus N_2 at 77 K	Equivalent.
TGA	Mettler Toledo TGA/DSC 1 Star ~20 mg, 30–1000 °C 10 °Cmin^{-1}	Netzsch STA 449 F3 ~120 mg, 24–1350 °C, 10 °C min^{-1}	Different instrument and sample mass.
SEM-EDS	Hitachi SU7000 FEG-SEM Oxford Instruments Ultim Max 170; 15 kV	Hitachi TM2020, Bruker Quantax 70; 15 kV	Different spatial / analytical resolution.
XRD	Bruker D8 Advance, LYNXEYE Detector	Bruker D2 Phaser, LYNXEYE Detector	Different instrument, geometry, resolution, background.
Powder Rheometry	Freeman FT4	Freeman FT4	Equivalent

identify relatively large-scale compositional heterogeneity, and there was no attempt to demonstrate homogeneity at a length-scale which could not be reasonably achieved by the instrument. It was therefore determined that the wet route measurements remained suitable for identifying elemental variation at the scale represented in the maps.

The XRD data for the dry- and wet-route samples were collected using two different laboratory diffractometers with a differing instrument flux and resolution. Differences in instrument optics and geometry may influence peak broadening, background characteristics, and phase abundances obtained by Rietveld refinement. Both datasets were collected using Cu-kα radiation and evaluated using consistent reference structures across a common 2θ range, allowing the principal crystalline phases in each sample to be identified. In the absence of a common reference analysed on both instruments, the refined phase assemblages of samples analysed on different instruments cannot be confidently compared with one another. Therefore, qualitative comparisons are restricted to the internally consistent dry-route dataset while the wet route dataset is reported and interpreted independently.

2.2. Samples

The experimental programme consisted of the initial production of a simplified Ce-doped zirconolite (D1 and W1), which were used to establish the processing behaviour of the respective synthesis routes. This was followed by trials which incorporated the baseline doped compositions for the dry route (D2, D3) and the wet route (W2), which included gadolinium and hafnium neutron absorbers and a Ti/Hf buffer phase. Because each material requires verification of different characteristics for use at plant-scale, the characterisation program was not identical for every sample. A detailed upstream powder characterisation was concentrated on D1 and W1 including determination of flow and particle characteristics, while samples D2, D3, and W2 acted to evaluate the resulting baseline-composition ceramics.

A summary of samples is given in Table 2.

2.3. Variations in target composition and co-milling approaches

To test the viability of the dry powder processing approach, an initial trial (D1) involved a 'simplified' target composition of $(Ca_{0.8}Ce_{0.2})(Zr_{0.9}Ce_{0.1})(Ti_{1.6}Fe_{0.4})O_7$, while two subsequent trials (D2 and D3) adopted the NDA baseline composition previously referenced. The final stage of powder processing, prior to pelletisation, was co-milling of the single zirconolite-rich precursor and CeO_2. This was delivered using planetary milling in trials D1 and D2, whereas a ball milling approach was used in D3. The use of yttria-stabilised zirconia (YSZ) milling media, and zinc stearate as a milling aid (at 0.5 wt.% of the weight of the powder charge) was common to all three trials.

To test the viability of wet powder processing route, initial investigations were used to test the viability of the approach with a $CaZrTi_2O_7$ composition (W1), while the NDA baseline composition was adopted in W2. In both W1 and W2, the final stage of powder processing, prior to pelletisation, involved a 'slurry' approach: powder planetary milled using YSZ milling media, with IPA added as a milling aid, and subsequent drying of the milled slurry.

Table 2
Experimental matrix summarising the compositions, processing routes, and characterisation methods applied to each trial.

Trial	Route	Target	Milling	Characterisation
D1	Dry	Simplified Ce-doped zirconolite: $(Ca_{0.8}Ce_{0.2})(Zr_{0.9}Ce_{0.1})(Ti_{1.6}Fe_{0.4})O_7$	Planetary co-milling with CeO_2	PSD, SSA, SEM, XRD, FT4, pellet density, SEM-EDS, XRD
D2	Dry	Baseline Ce/Gd/Hf/Fe-doped zirconolite +5 wt. % Ti/Hf buffer see NDA 'baseline' in Section 1	Planetary co-milling with CeO_2; Zn stearate milling aid	Pellet density, SEM-EDS XRD
D3	Dry	Baseline Ce/Gd/Hf/Fe-doped zirconolite +5 wt. % Ti/Hf buffer see NDA 'baseline' in Section 1	Two-stage ball mill CeO2 initially milled for 4 hrs followed by precursor addition and further 4 hrs.	Pellet density, SEM-EDS XRD
W1	Wet	Simplified $CaZrTi_2O_7$ process-development composition	Planetary milling in IPA up to 135 min.	PSD, SSA, TGA, SEM, XRD, FT4
W2	Wet	Baseline Ce/Gd/Ff/Fe-doped zirconolite +5 wt, % Ti/Hf buffer see NDA 'baseline' in Section 1	135 min planetary co-milling in IPA with CeO_2/HfO_2/Ti-Hf buffer.	Pellet density, SEM-EDS XRD

2.4. Reagent oxides

The dry route work used the following oxide powders: $CaTiO_3$ (>99 %, Thermo Scientific), TiO_2 (anatase, 99.8 %, Sigma-Aldrich), ZrO_2 (99.6 %, Sigma-Aldrich), Fe_2O_3 (99.9 %, Thermo Scientific); the Hf and Gd components in D2 and D3 were from HfO_2 (99 %, Thermo Scientific) and Gd_2O_3 (99.9 % REacton™, Thermo Scientific). A single type of CeO_2 (99.9 % REacton™, Thermo Scientific) was used in both the wet and dry routes (D1, D2, D3 and W2), while the Hf and Ti/Hf buffer component of W2 used HfO_2 (99.9 %, Alfa Aesar) and TiO_2 (99.9 %, Thermo Scientific).

All reagent oxides were weighed and handled under argon (Ar), unless otherwise stated. The Ti-Hf buffer phase, which was used to mediate the formation of perovskite, was synthesised by heat treating the HfO_2 and TiO_2 in air at 800 °C and mixing stoichiometric proportions of these to match the chemical composition $(TiO_2)_{0.9}(HfO_2)_{0.1}$, before homogenisation. Once prepared, the material was handled under Ar.

2.5. Particle size analysis

PSD measurements were collected using a Malvern Panalytical Mastersizer 3000 with a Hydro EV unit with a deionised water dispersant and ultrasonication. The distributions reported in this publication represent the mean of 10 measurements, assuming a particle refractive index of 2.34, absorption index of 0.01, and a dispersant refractive index of 1.33. Powder distributions were interpreted on the basis that the application of high shear and ultrasonication would have caused loose agglomerates to readily break up, and so the coarse fractions reported were assumed to represent strong agglomerates or fragments which could not be dispersed.

2.6. Specific surface area

SSA was measured using the Brunauer-Emmett-Teller method which determines surface area from the absorption isotherm of an insert gas by applying a multilayer absorption model over a defined relative pressure range. The SSA was determined using a Micromeritics TriStar II Plus instrument, using N_2 as the adsorptive at 77 K. Adsorption isotherms were collected over the relative pressure range c. 0.05 P/Po through 0.3 P/Po. Before testing, samples were purged at 110 °C under a constant flow of N_2 for 24 h to eliminate surface-adhered water and species.

2.7. Thermogravimetric analysis

TGA measurements on the dry route powders were carried out using a Mettler Toledo TGA/DSC 1 Star System operated in pure TGA mode (DSC signal disabled): circa. 20 mg of each sample was dispensed into an unlidded alumina crucible before being heated in the temperature range 30 °C through 1000 °C (ramp 10 °C/min). For the wet route powders, measurements were performed using a NETZSCH STA 449 F3 in the temperature range 24 °C through 1350 °C at a heating rate of 10 °C/min on circa. 120 mg of sample.

Mass change was normalised to the initial specimen mass and is reported as wt.%. The TGA data were used primarily to identify the presence and approximate target ranges of mass-loss events within each material. Due to the differing masses of each sample and instrumentation used for the two routes, the profiles were not used for direct like-for-like comparison of decomposition kinetics, including the precise onset, breadth, or rate of individual events. Where mass-loss regions are associated with possible decomposition processes, these assignments are based on comparison with literature reported temperature ranges, and are treated as indicative, in the absence of evolved gas analysis. Any statistics reported are based on each individual assessment of each profile and are given solely as approximate indications.

2.8. Powder rheometry

The 'confined flow' methodology of a Freeman FT4 powder rheometer was used for both dry route and wet route powders. This approach involves determining the amount of energy required for a helical blade to traverse a conditioned powder bed. A 50 mm dia. glass vessel was filled with circa. 50 cm^3 of specimen and subjected to six conditioning cycles at a blade speed of -100 mm·s^{-1} to form a homogeneous powder bed free of entrapped air, prior to testing at progressively reducing blade speeds of -70 mm·s^{-1}, -40 mm·s^{-1}, and -10 mm·s^{-1}.

2.9. Scanning electron microscopy and energy dispersive X-ray spectroscopy

Before analysis, powders were deposited onto a carbon sticky pad with excess powder removed using compressed air. Sintered pellets were cut from the solidified material and vacuum impregnated with resin. In both cases (powders and pellets) a carbon coat was applied to the surface. A Hitachi SU7000 FEG-SEM, plus Oxford Instruments Ultim Max 170 EDX, was used for the dry route samples, whereas the wet route work utilised a Hitachi TM3030 SEM and Bruker Quantax 70 EDX. A 15 kV accelerating voltage was used for both analyses.

The spatial resolution of the SEM-EDS mapping is governed by the electron interaction volume within the specimen, and therefore depends on the composition, geometry, and instrument operating conditions, and it is not possible to assign a single fixed value specific to the detector. Therefore, we cannot confidently provide a precise spatial resolution for the EDS measurements reported here though it is acknowledged that the TM3030 and Bruker QUANTAX instruments used for the wet-route system have a reduced spatial resolution relative to the SU7000 FEG-SEM, and so the elemental maps resulting from the W2 pellet can only strictly be interpreted in terms of chemical variation at the micron length-scale. No direct comparison is therefore attempted here.

2.10. Powder XRD and crystal structure refinement

For dry route samples, diffraction data were collected using a Bruker D8 Advance equipped with a LYNXEYE detector ($5° \leq 2\theta \leq 130°$), while wet route data were collected using a Bruker D2 phaser ($10° \leq 2\theta \leq 100°$), also equipped with a LYNXEYE detector. For analysis, a common range of $10° \leq 2\theta \leq 90°$ was used in all cases to assist with visualisation of fingerprint zirconolite reflections expected at circa. 25–35°2θ, with Cu-Kα radiation used in both cases.

Crystal structure refinement was performed using the Rietveld crystal structure refinement method [9], with diffraction patterns fitted using Bruker DIFFRAC.TOPAS. The instrument background was fitted using a 5th order Chebyshev polynomial and peaks fitted using the fundamental parameters approach. The reference structures used for the analysis are provided in Table 3. Gaussian and Lorentzian convolutions for crystallite size and strain were included to improve the profile fit, though measurements of these were not interpreted here. Relative phase abundances were reported in wt.% for each sample separately.

It is likely that differences in instrument configuration will have influenced the shape of each peak, the instrument background, and the signal intensity, and therefore have affected the quantitative phase fractions obtained by crystal structure refinement. The phase abundances obtained for the dry- and wet-route materials can therefore only be reported as independent quantitative results and cannot be used to calculate absolute differences in phase abundance between the two routes.

2.11. Pellet density

The densities of the sintered pellets were determined using the Archimedes method, and samples were weighed in air and while suspended in water to evaluate the apparent sample volume by buoyancy. Measurements were performed in triplicate and the mean values are reported; the measurement of scatter reported corresponds with the standard deviation of the dataset.

3. Synthesis and characterisation of zirconolite-rich precursor powders

For the dry route, an off-stoichiometric formulation

Table 3
Reference structures for crystal structure refinement.

Phase	Composition	Ref
Zirconolite-2M	$CaZrTi_2O_7$	[10]
Zirconolite-3T	$CaZrTi_2O_7$	[11]
Perovskite	$CaTiO_3$	[12]
Rutile	TiO_2	[13]
Anatase	TiO_2	[14]
Pseudobrookite	Fe_2TiO_5	[15]

$Ca_{0.8}Zr_{0.9}Ti_{1.6}Fe_{0.4}O_7$ (D1) was specified to accommodate subsequent CeO_2 during later processing and to maintain the stability of the zirconolite under solid state synthesis conditions. For D2 and D3 the Ti/Hf buffer was chosen to be incorporated into the single precursor and was not added in the co-milling stage with CeO_2 which was determined to be more desirable at plant-process scale. Thus, for D2 and D3 the off-stoichiometric composition was updated to 95 wt.% $(Ca_{0.785}Gd_{0.015})(Zr_{0.75}Gd_{0.015}Hf_{0.1})(Ti_{1.6}Fe_{0.4})O_7$ plus a 5 wt.% $(Ti_{0.9}Hf_{0.1})O_2$ buffer. The wet route initially targeted stoichiometric zirconolite $CaZrTi_2O_7$ in order to establish phase formation behaviour prior to the introduction of compositional changes and neutron absorbers and the Ti/Hf buffer. As both routes were eventually aimed to target the same baseline composition (D2, D3 and W2), it was determined that small differences in initial cation ratios did not compromise the validity of the assessment.

A significant focus of the present work was evaluating how the properties of the Ce-containing sintered pellets evolved from the immediately upstream co-milled powder. Nonetheless, in acknowledgement that an understanding of these characteristics might benefit from a more detailed knowledge of the further upstream 'as-produced' zirconolite-rich powders, a limited selection of characterisation was carried out on the D1 powder, as well as the W1 powder (including its 'intermediate' stir-dried and calcined versions).

3.1. Dry route synthesis

The process of zirconolite synthesis via a dry physical route is well established [16]; in this case it was decided to produce the single zirconolite-rich precursor powder by pulverisation of previously-sintered pellets, these having already been synthesised from reagent oxides. A pair of 1 L high density polyethylene (HDPE) mill jars were each charged with 280 g of the reagent oxides and yttria-stabilized zirconia (YSZ) milling media added (320 g 5 mm dia. balls and 900 g 10 mm dia. cylinders). The media and powder were covered with 200 g of IPA as a milling aid, and the jar placed on a two-tier roller mill for 8 hrs. The slurry was decanted onto a ceramic dish, dried for 12 hrs in air at 80 °C to evolve the solvent and passed through a 500 μm sieve to separate the media and recover the powder.

The (presumed to be) zirconolite-rich powder (Ca-Zr-Fe-Ti oxide in D1 trial; Ca-Zr-Fe-Ti-Gd-Hf-(Ti/Hf) oxide in the D2 and D3 trials) was subsequently pressed into pellets at a pressure of 382 MPa (30 kN, 60 *sec*.): pellets were placed on a ZrO_2 sheet and covered in a layer of ZrO_2 powder to prevent adhesion, and stacked and covered before being sintered in air: ambient temperature (circa. 25 °C) to 1300 °C at a ramp rate of 10 °C/min; 5 h dwell at 1300 °C; ramp-down to ambient, again at 10 °C/min. Adhered powder was removed before pellets were crushed using a hammer mill and ground using a cobalt-bonded tungsten carbide Tema disc mill to a target particle size of 100 μm; the resulting material is (in each case) the single zirconolite-rich precursor (D1, D2, D3) that was intended to be co-milled with CeO_2 at a later stage.

3.2. Wet route synthesis

To produce a simplified target composition of $CaZrTi_2O_7$ (W1) [17], ethanolic solutions of $Zr(OC_3H_8)_4$ and $Ti(OC_2H_7)_4$ were weighed and hydrolysed in a 2 L borosilicate glass beaker by the addition of aqueous $Ca(NO_3)_2$ solution and stir-dried (92 °C at 400 rpm) using a Fisherbrand Isotemp hotplate. This formed a precipitate which contained a mixture of the cations required to form zirconolite in the appropriate stoichiometry, though it was not expected that this would match the crystal structure of the desired phase at this point. The resulting dried precipitate was calcined at 800 °C for 12 h to decompose the organic solid to form a metal oxide mixture. At this stage (and with a lookahead to informing the later W2 work), there was also an aim to optimise the powder milling conditions. As such, the calcined Ca-Zr-Ti oxide precursor was then planetary milled at 400 rpm, in YSZ-lined milling jars with 70 g of 3 mm YSZ milling media and an IPA carrier fluid; this milling was performed in increments of 15 min for a total of 60 min initially, then an extension to 135 min.

A similar approach was utilised for the baseline composition (W2). Ethanolic mixtures of $Zr(OC_3H_8)_4$ and $Ti(OC_2H_7)_4$ were prepared to the target stoichiometry, while an aqueous solution of $Ca(NO_3)_2$, $FeNO_3$, and $GdNO_3$ was used to hydrolyse the reagents. This formed a solid precipitate with the required stoichiometry. Using the same conditions as in the W1 approach, the Ca-Zr-Ti-Fe-Gd precipitate was then dried and calcined.

3.3. Particle size analysis

The D1 powder (Fig. 1) reported a broad distribution with three identifiable features. To probe the location of these, deconvolution of the distribution was performed by fitting a series of Gaussian peaks in the log-10 space. The analysis reported a fine population (circa. 3.69 μm), an intermediate population which caused the internal shoulder to form (circa. 24.4 μm), and a coarse population (circa. 103 μm) which caused the second mode, though due to the x axis scaling it was challenging to quantify the relative proportions of these fractions. Deconvolution did not successfully fit an extremely fine potential shoulder which appeared in the <1.0 μm range.

This can be interpreted as being consistent with a powder generated through sequential mechanical processing. Sintering after blending of reagent oxides will have likely caused the formation of zirconolite grains (individual microscopic zirconolite crystals) with sizing dependent on the sintering temperature, dwell time, and additives [18]. Grain boundary interfaces act as preferential pathways for crack propagation during milling [19] and these are randomly sized due to curvature-driven grain growth [20]; further milling reduced the size of large fragments, generating a micron- to sub-micron population. The coarse mode could also have been formed because of re-agglomeration of these finely divided particles. However retention of this mode in spite of wet dispersion and ultrasonication suggested that these larger particles could not be separated, and hence it was likely the case that these consisted of large solid fragments.

The PSD of the W1 powder after drying, calcining (at 800 °C), and subsequent milling for 60 and 135 min was also measured, and these results are shown in Fig. 2. The stir-dried precipitate contained a bimodal distribution with a dominant coarse fraction which remained after calcination. Following this, the intermediate mode decreased in size: this behaviour is consistent with redistribution of an intermediate agglomerate population rather than a uniform shift in particle size. Alternatively, the intermediate population was comprised of dispersible clusters which underwent incipient consolidation during calcination (i.e., strengthening of interparticle contacts), such that they were no longer dispersed under the PSD measurement conditions, and instead these contributed to the coarse mode (though this remains a tentative interpretation without further data).

The coarse mode was dispersed on milling, consistent with an interpretation that these consisted of relatively hard agglomerates which coalesced during stir drying and which were not easily broken down by agitation. When milled, a distinct peak developed at circa. 0.5 μm with an additional shoulder at circa. 0.1–0.2 μm, while a separate population centred at circa. 2 μm appeared with a weak shoulder at circa. 8–10 μm. The appearance of multiple populations indicated that the powder did not undergo uniform fragmentation, but instead had a behaviour dependent on particle sizing, consistent with a mechanically heterogeneous microstructure in which different regions responded differently to the mill. The generation of fines and persistence of coarser PSD shoulders suggests that fragmentation and re-agglomeration may have occurred concurrently, and this was likely confirmed in the PSD collected after 135 min of milling.

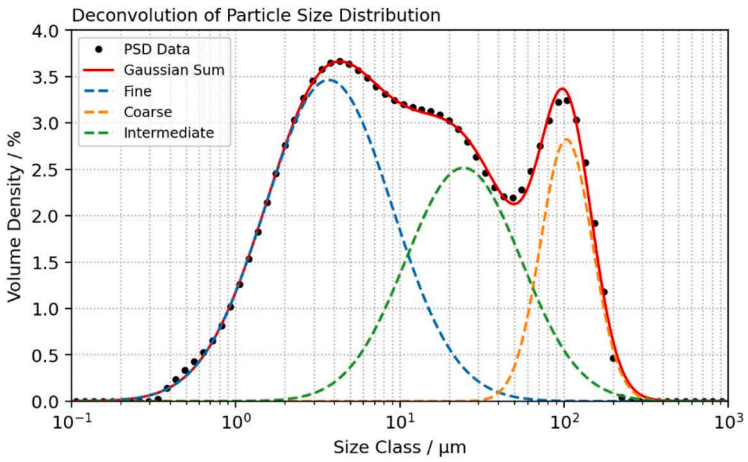


Fig. 1. Deconvolution of the particle size distribution of the D1 powder.

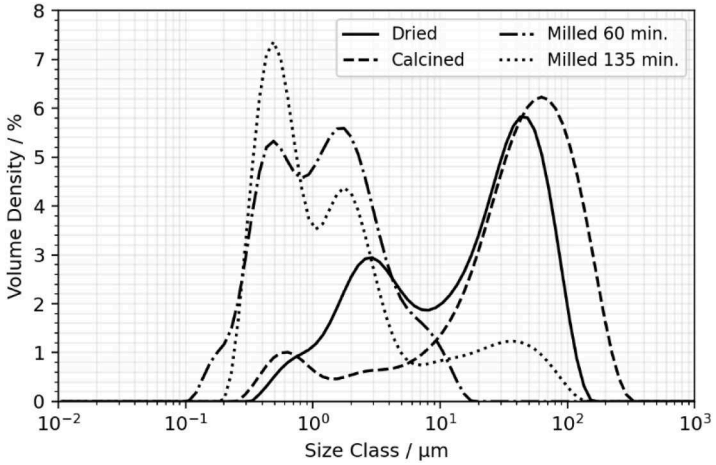


Fig. 2. Particle size distribution of the different stages of synthesis of the W1 powder.

3.4. Specific surface area

The SSA of the D1 powder, as well as the calcined (but un-milled) version of the W1 powder, are reported in Table 4. The wet route reported a significantly higher SSA, consistent with finer particle grading and a greater degree of powder roughness. This suggests that the powder may have a higher reactivity, a greater capacity for adsorbing moisture, and a stronger driving force for sintering due to a greater surface energy. These features may be beneficial for enabling complete sintering and densification at a lower temperature, though may also increase the sensitivity of the wet route powder to agglomeration, poor flow characteristics, and secondary phase formation caused by surface-driven effects.

3.5. Morphology

PSA and SSA data can provide bulk measurements of particle properties, but provide little information about the nature of the physical particle geometry (e.g., shape, agglomerate structure). Therefore, backscattered electron (BSE) images were collected. Results for the D1 powder are shown in Fig. 3, and the stir-dried stage of the W1 powder in Fig. 4.

Table 4
Specific surface area of the wet route powder after calcination, and the dry route powder.

Powder	SSA m^2g^{-1}
D1	1.67
W1 (after calcination at 800 °C)	12.98

The D1 powder had a coarse, granular morphology, populated with fragments extending to hundreds of µm. The faceted fracture surfaces are consistent with the comminution of a previously consolidated, dense material (i.e., the upstream sintered pellets), supporting the interpretation that the coarse fraction observed by PSD (Fig. 1) consisted of mechanically robust fragments rather than weak agglomerates. A second population of finer particles was observed scattered within the larger fragments, consistent with cleavage- or attrition-derived fines which were adhered to fracture surfaces.

Backscattered electron images of the stir-dried wet route precipitate are shown in Fig. 4, and indicated a heterogeneous powder morphology consistent with the PSD. At a higher magnification, particles appeared to have comprised of fractured and cracked agglomerates, consistent with drying-induced shrinkage. Finer particles adhered to the surface of larger agglomerates, in some cases forming local bridges between particles, suggested that secondary materials may have also contributed to the cohesion of particles. While these agglomerates appear structurally intact at the length-scales examined, their cracked morphology and the absence of visible necking suggests that they remained mechanically weak and it is likely that these could have been separated under a fairly low applied stress.

Electron images of the W1 powder after calcining at 800 °C are

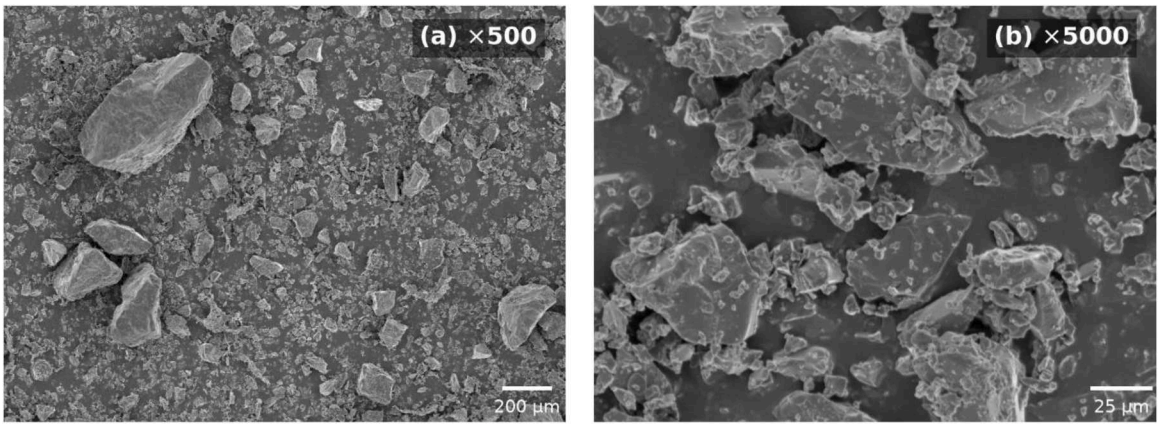


Fig. 3. Backscattered electron images of the D1 powder at × 500, and × 5000 magnification.

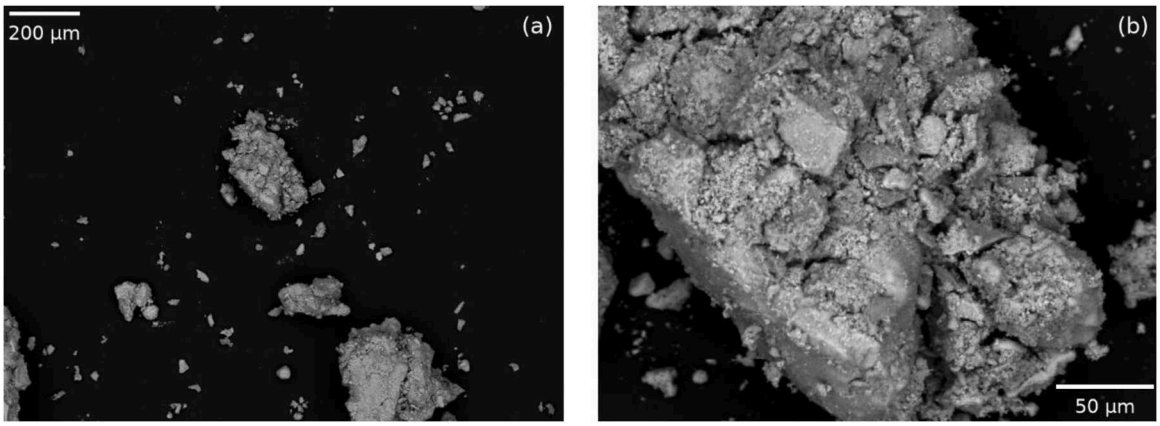


Fig. 4. SEM-EDS backscattered electron imaging data for the stir-dried intermediate version of the W1 powder. BSE data collected at × 120 magnification is shown in (a), and at × 800 magnification in (b).

shown in Fig. 5. These results indicated that large particles retained shrinkage-related cracking and drying-derived agglomerate structures which had persisted after calcination, consistent with the data reported by the PSD. At higher magnification, fine material adhered to the surface of larger particles, while the larger particles appeared smooth and faceted, consistent with local densification. There was no clear evidence of interparticle necking between the adhered fines. The SEM data can provide only a local field of view, and sample mounting may have biased the association of fine and coarse material. Therefore, these observations can only be taken qualitatively and in conjunction with the bulk PSD, and this interpretation would benefit from an instrument capable of achieving a higher spatial resolution for comparison between the W1 and D1 samples.

Following milling, powder SEM (shown in Fig. 6) data became more challenging to interpret due to limited particle coverage on the adhesive substrate and limitations in image focus, such that the observed fields may not be completely representative of the bulk powder. However, a small number of coarse particles >100 µm were observed, although the dominant features comprised dispersed clusters of finer material with comparatively smooth, rounded morphologies, rather than angular

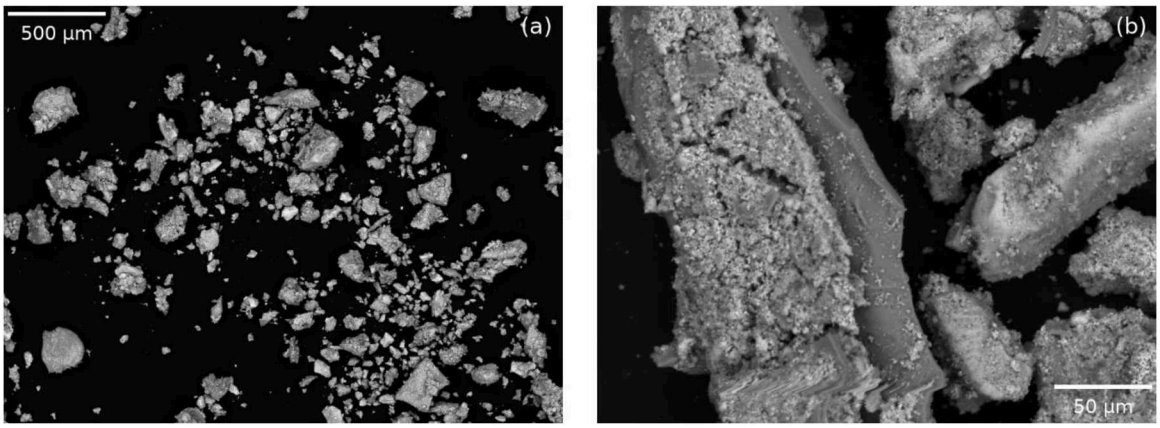


Fig. 5. SEM-EDS backscattered electron imaging data for the 800 °C calcined W1 powder, captured at × 100 magnification in (a) and at × 1000 magnification in (b).

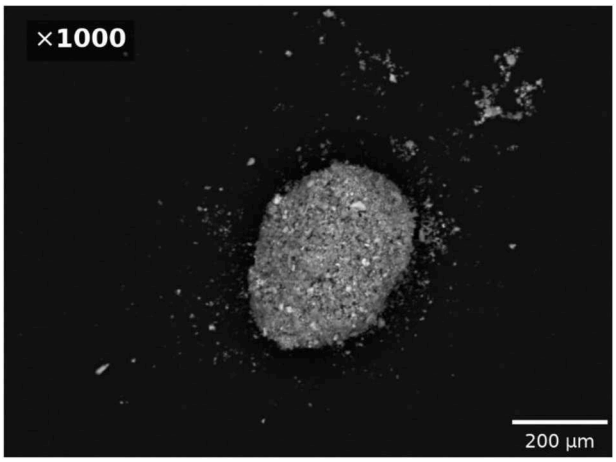


Fig. 6. Backscattered electron images for the W1 powder after 60 min of milling.

fracture fragments. These clusters are consistent with secondary agglomeration of fines following thermal treatment and provide a plausible explanation for the coarse fraction which re-emerged in the PSD. While challenging to observe, the partial scattering of these is also consistent with coexisting fine and intermediate peaks in these results, though similarly, further analysis of these samples is not possible in the absence of an instrument with a higher spatial resolution.

3.6. X-ray diffraction and phase assemblage

The backscattered electron images and PSD data suggested that the powders exhibited agglomeration behaviour that evolved with processing history, though these results cannot be used to fully interpret chemical characteristics. To assess the phase assemblage through each processing route, XRD was used to identify crystalline phases present in what at this point was assumed to be the zirconolite-rich powders.

Profile data for the D1 powder are reported in Fig. 7. The profile data and refinement results suggested that zirconolite-2 M was the dominant phase: 89.7(2) wt.% zirconolite-2 M with the bulk composition $CaZrTi_2O_7$ with minor additional contributions from a perovskite ($CaTiO_3$; 4.1(7) wt.%) phase as well as pseudo-brookite (Fe_2TiO_5; 6.6(2) wt.%). Given that the material was intentionally off stoichiometry, the presence of minor secondary phases was expected, and it is plausible that this reflects local compositional heterogeneity and incomplete cation incorporation.

XRD patterns were also collected for the W1 material and are reported in Fig. 8, with patterns collected after stir-drying in plot (a), after calcining in plot (b) and after milling for 135 min in plot (c). The stir-dried material was found to be significantly X-ray amorphous, with no discrete Bragg reflections, and no indication of any zirconolite. The profile shape was consistent with the principal reflections of TiO_2 anatase [14,21], being dominated by a high-intensity, broad diffuse maximum at ~25.5° 2θ which was attributed to the 101 reflection, suggesting the presence of anatase-like short-range order (i.e., highly disordered or nanocrystalline anatase) within an otherwise amorphous structure. It has previously been demonstrated that short-range structural order or disorder is can significantly influence subsequent crystallisation behaviour during sintering [22].

Calcination of the stir-dried wet route precipitate appeared to produce a zirconolite phase, alongside rutile [13] and $CaTiO_3$ perovskite [12]. Fingerprint reflections are shown in the circa. 30° 2θ range, though were sufficiently broad to merge groups into single peaks, indicating a high degree of disorder in the zirconolite formed. The positions of both zirconolite-2 M [10] and zirconolite-3T [11] are also reported, with the 3T phase indicated through the presence of a low-intensity peak at 25.27° 2θ in Fig. 8(b) and 25.35° 2θ Fig. 8(c) which could not be attributed to any other viable phase. Rutile is consistent with the crystallisation of the metastable anatase during sintering, and this process has been previously shown to have an onset temperature of circa. 400 °C and further acceleration over 600 °C [23], consistent with the process here.

3.7. Thermogravimetric analysis

TGA was used to probe the extent of decomposition and identify residual volatiles in the undoped zirconolites. The TGA results, from ambient temperature up to 1000 °C, for the D1 powder and the stir-dried version of the W1 material, are given in Fig. 9. The difference in specimen mass between the two measurements was likely to have affected the thermal response of the powders, as previously discussed, which will have changed the onset, breadth, and shape of each mass loss event in Fig. 9. The profiles therefore cannot be interpreted as directly comparable measurements, and should be considered in independently from one another, including the magnitude and the temperature range in which each event occurs.

The D1 powder reported a total mass loss of circa. 0.29 wt.%, consistent with a highly crystalline material (low SSA, few surface

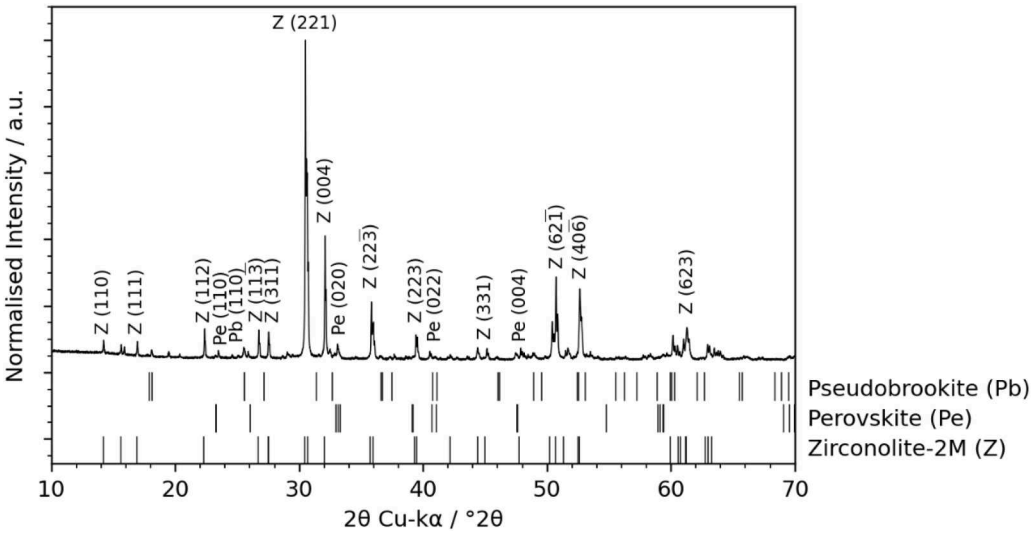


Fig. 7. Diffraction profile of the D1 powder.

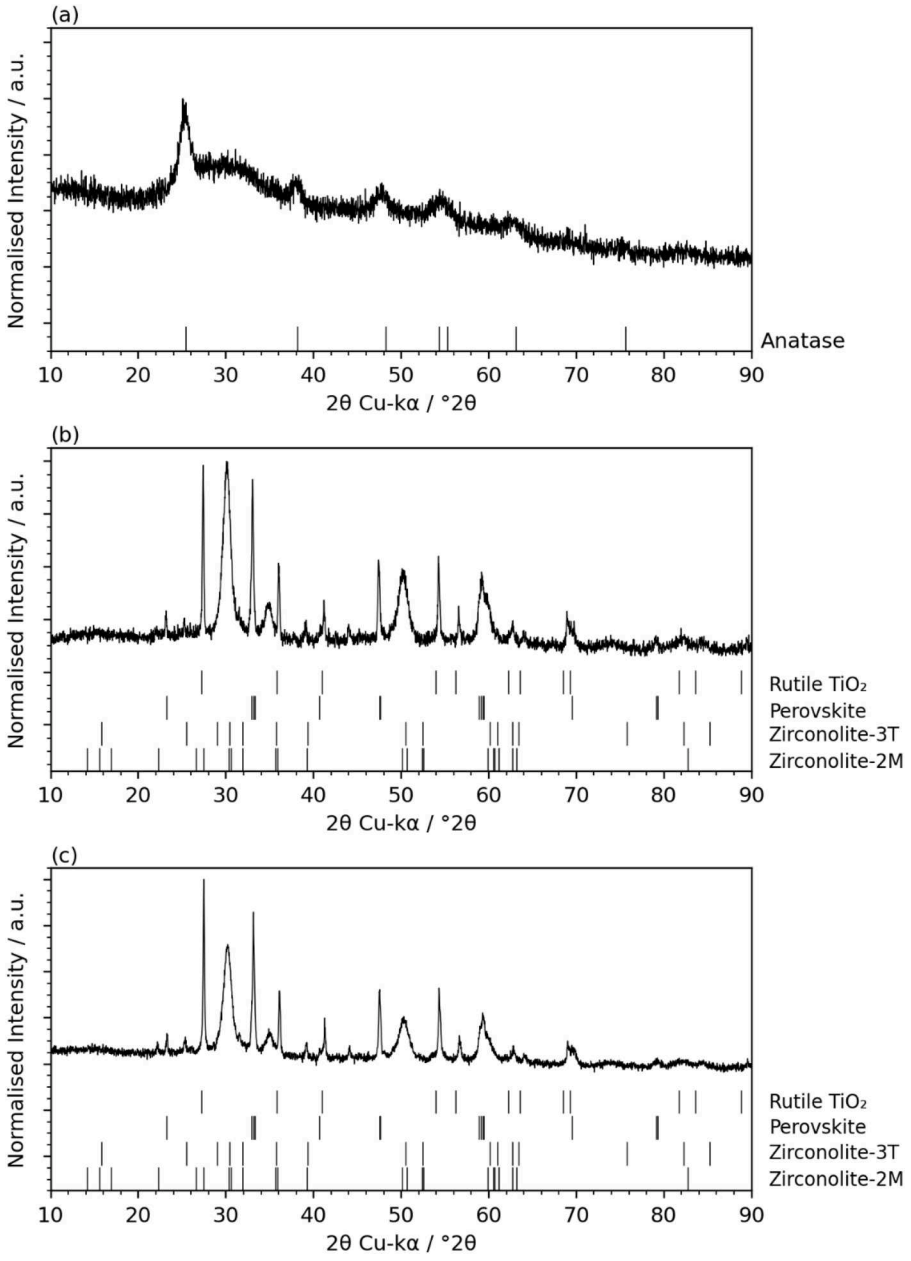


Fig. 8. Diffraction profile of the W1 material after stir drying (a), subsequent calcining (b), and subsequent milling (135 min) (c). The position of theoretical peaks >5 % max. are reported.

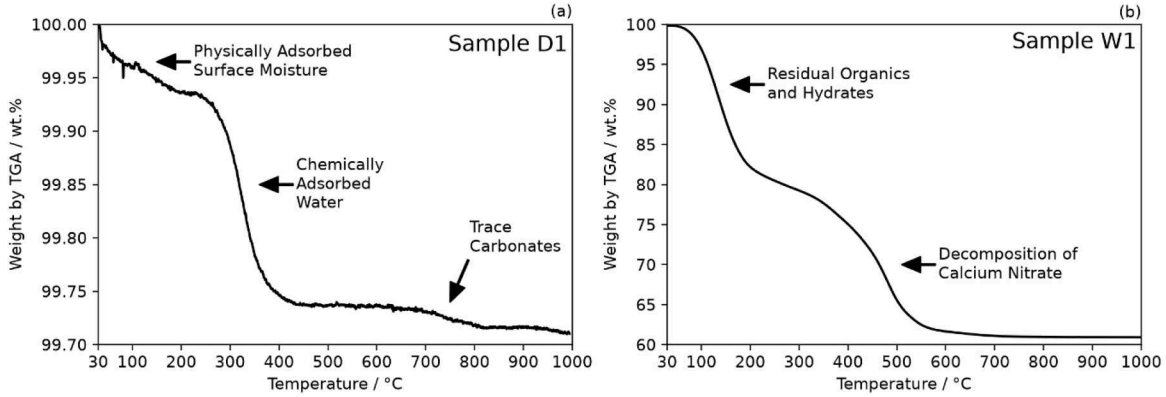


Fig. 9. Thermogravimetric analysis data for the D1 powder (a) and the precipitated version of the W1 material (b).

defects, low surface reactivity). In the literature, losses below circa. 150 °C are often attributed to the expulsion of physically adsorbed surface moisture [24,25]. The most prominent loss occurred at between circa. 250 °C and 450 °C and the literature has previously attributed decompositions in this range to the loss of chemically adsorbed water [26]. Based again on the literature, the final, very low wt.% loss between 650 °C and 850 °C could potentially be attributed to loss of carbonates [27].

To improve confidence in this discussion, all these interpretations require a technique sensitive to the evolved gas composition (evolved gas analysis; EGA) which was not carried out in the present work. However, the theorised presence of only trace surface-bound volatiles in the D1 powder does propose the formation of a stable structure alongside a reduced risk of gas evolution during consolidation, and improved predictability in processing.

The W1 material reported two clear regions of mass loss, reaching a total loss of circa. 38 wt.% by 1000 °C. It is possible that the stir-dried precipitate may have retained a volume of residual organics and hydrates following synthesis, with circa. 20 wt.% of the initial mass lost between 30 °C and 200 °C, and according to the literature this temperature range is consistent with the removal of physically retained water and other volatile species associated with the precursor chemistry [28]. Between 200 °C and 400 °C continued mass loss was observed over the temperature range in which, as reported elsewhere, decomposition of residual alkoxide-derived organic species might be expected in samples similar to these [29]. A further mass loss between 400 °C and 600 °C could be theorised as being consistent with the reported decomposition of calcium nitrate as extensively reported [28,30,31].

Similarly to the D1 specimen, as EGA was not performed here the chemical species associated with these individual mass loss events could not be directly identified and these assignments should be regarded as tentative. However, the substantial overall mass loss confirms the presence of volatile decomposable species within the wet-route precursor, the removal of which during heating is likely to modify particle morphology and surface chemistry. This itself may influence particle cohesion and flow behaviour.

3.8. Confined flow behaviour characteristics

To quantify the powder response under conditions of confined flow, the flow properties were analysed using the FT4 method (Section 2.8). It is likely that poor flow characteristics could lead to arching, ratholing, intermittent discharge, and localised segregation, and in turn compromise uniformity and the viability of the process.

Powder rheometry was performed on the D1 and W1 materials to assess the handling behaviour of the single zirconolite-rich precursor at the stage at which it would be fed into a theorised future processing facility; from an industrial perspective this was determined to be the point of most significant interest. However, the D1 and W1 materials still represent simplified compositions used during process development,

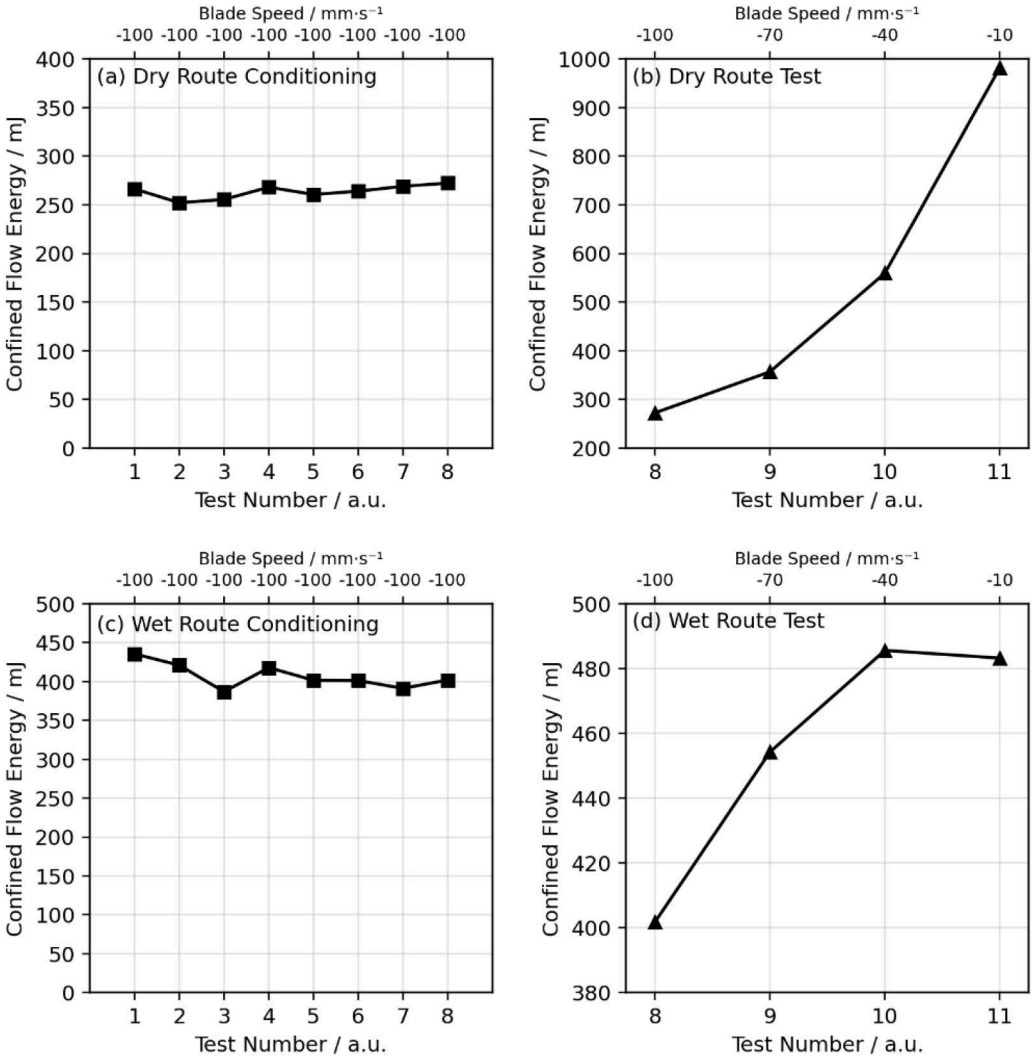


Fig. 10. FT4 confined flow data for D1 (a and b), and the 135 min milled version of W1 (c and d).

and incorporation of additional components present in the baseline precursor formulations may subsequently density, surface chemistry, particle size distribution, and agglomeration behaviour. The FT4 results should therefore not be assumed to strictly represent those of D2/D3 or W2, which require further characterisation.

Fig. 10 shows the evolution of total energy with successive FT4 test cycles, where the initial eight measurements at a constant 100 mm·s^{-1} (in Fig. 10(a) and Fig. 10(c)) correspond to conditioning. For both materials, there is modest variation in confined flow energy over the conditioning steps, indicating that the powders are relatively stable, and not experiencing significant agglomeration or de-agglomeration. The BFE (the energy value on the final conditioning step) of the dry route powder is approximately 280 mJ; this is lower than the circa. 400 mJ of the wet route powder which implies that the former flows more easily in these specific conditions (i.e., less energy required to displace the same volume of powder). However, varying the blade speed (in Fig. 10(b) and Fig. 10(d)) results in an increase in energy in both materials, especially so in the D1 material, where energy increases by circa. 700 mJ over the variable speed test range (in contrast to a circa. 80 mJ increase in the W1 powder). Thus, it is evident that the dry route powder is significantly more sensitive to changes in the flow rate.

The W1 material reported a change in total energy as the tip speed was reduced from 100 to 10 mm·s^{-1} and approached a plateau at the lowest speed. It is suspected that at high tip speeds powder flow became governed by bed friction, rather than by the shear rate, and once the network was fully developed, further reduction in the shear rate produced only a limited additional increase in flow energy; once the bed was developed, the instrument no longer needed to work harder to maintain flow. By contrast, the D1 material showed no such plateau; this might indicate that the resistance to flow remained more strongly dependent on shear conditions, and this is consistent with a structure dominated by interlocking fragments rather than agglomerates. Both tests were carried out in a matching instrument with consistent parameters.

4. Synthesis of Ce-doped zirconolite

The next stage in processing involved consolidation of the doped powders by CPS to form full zirconolite ceramics. In theory this could (and may in practice) be replaced by HIP [32,33], though for simplicity a CPS route was used here, and it has previously been suggested that differences introduced during powder synthesis and homogenisation at this point could be carried through into the final microstructure [34].

4.1. Dry route

In both D1 [Ca-Zr-Ti-Fe oxide] and D2 [Ca-Zr-Ti-Fe-Gd-Hf-(Ti/Hf) oxide], the zirconolite-rich powder was co-milled with CeO_2 using a planetary milling approach. This involved 200 g of powder (total), plus 0.5 wt.% zinc stearate as a milling aid, milled in a Fritzsch Pulverisette 6 single jar planetary mill charged with 300 g of 5 mm dia. YSZ milling media. The mill was run at 500 rpm for a total of 20 cycles, and each cycle involved running the mill for 5 min in the forward direction, before the mill pot was allowed to cool for 45 min, with the mill then run in the reverse direction.

There was some interest in determining if alternative milling approaches could have an influence on the properties of the downstream sintered ceramic. As such, for trial D3 [again Ca-Zr-Ti-Fe-Gd-Hf-(Ti/Hf) oxide] an alternative 'two-step' ball milling approach was used: a three-tier Capco roller mill was utilised, with 78 rpm rotation; milling used 1 l HDPE jars, charged with 320 g of 5 mm diameter YSZ balls and 900 g YSZ 10 mm pellets, with 300 g powder charge, and again 0.5 wt.% zinc stearate added at the co-milling stage. First, the required amount of CeO_2 was added to the mill jar and milled for four hours. The D3 zirconolite-rich powder (plus the zinc stearate) was then added to the mill jar, with another four hours of co-milling carried out.

The co-milled (that is, Ce-containing) powders, in D1, D2 and D3, were fed into a Specac Atlas Autotouch 15TA computer-controlled press with a ø10 mm steel die. Circa. 2 g of the powder in each case was pressed into a single pellet, with a pressure of 382 MPa (30 kN load) applied for 60 s. Pellets were placed on a zirconia plate with a layer of zirconia powder to avoid adhesion and were heated in air from ambient temperature at a rate of 5 °C per min. to a max. temperature of 1350 °C, followed by a 20-hr. dwell, then cooled back to ambient temperature at a controlled rate of 5 °C per. min. The sintered pellets were then stored under Ar.

4.2. Wet route

Using the same milling approach as W1 described earlier in Section 3.2 (135 min planetary milling, with IPA employed as a milling aid, and subsequent drying of the milled slurry), the calcined version of the W2 material [Ca-Zr-Ti-Fe-Gd oxide] was co-milled alongside CeO_2, HfO_2 and $(Ti_{0.9}Hf_{0.1})O_2$ powders, to the target stoichiometry. The resulting co-milled powder (after its slurry had been dried) was then passed through a 500 μm mesh sieve before being pelletised by under a uniaxial force of 3 t (~260 MPa) in a steel die, with pellets then sintered under equivalent conditions as the dry route pellets (sintering in air, with 20 h dwell at 1350 °C).

4.3. Pellet density and microstructure

Sintered pellets density values are presented in Table 5. All four examples exhibited a high density relative to a typical zirconolite, with the D2 being pellet notably higher in value than the other three; the density values are broadly in agreement with literature data for similar materials (e.g., [35,36]).

Pellet section SEM images are shown in Fig. 11 (D1, D2, D3) and Fig. 12(W2). The dry route pellets formed a dense zirconolite matrix containing four different microstructural features. A population of dark grains consistent with a minor lower density perovskite-type phase were found [37], embedded within a zirconolite bulk. The bulk had two apparent grain types, though no attempt was made to attribute either to a particular composition using these data as the technique was not sensitive to the crystal structure.

Selected distinct regions within the D2 and D3 pellets were evaluated by point EDS analysis, though equivalent analyses were not acquired for D1 or W2. It was found that four measurements from D2 and D3 gave closely grouped cation-normalised compositions of circa. $Ca_{0.70}Ce_{0.30}Zr_{0.80}Hf_{0.14}Fe_{0.38}$ for D2 and $Ca_{0.69}Ce_{0.32}Gd_{0.03}Zr_{0.78}Hf_{0.14}$, for D3, respectively.

These compositions are broadly consistent with the targeted doped zirconolite composition previously described. Two of the Ca-Ti-rich secondary regions which were found independently in each sample gave compositions of $Ca_{0.70}Ce_{0.23}Ti_{0.96}Fe_{0.09}Zr_{0.02}$ in D2 and $Ca_{0.69}Ca_{0.25}Ti_{0.95}Fe_{0.09}Zr_{0.02}$ in D3, though these cannot be used to attribute any particular phase to any particular proposed zirconolite or perovskite grain; this discussion is based only on compositional characteristics supported by EDS.

The wet route microstructure reported broadly similar features to the dry route, namely a matrix dominated by zirconolite containing discrete minor secondary inclusions and dispersed pores. The lower instrument resolution meant that it was not possible to resolve any grain-scale

Table 5
Densities of the D1, D2, D3, and W1 sintered pellets.

Sample	Density (g·cm^{-3})
D1	4.63(9)
D2	4.87(10)
D3	4.57(9)
W2	4.51 (2)

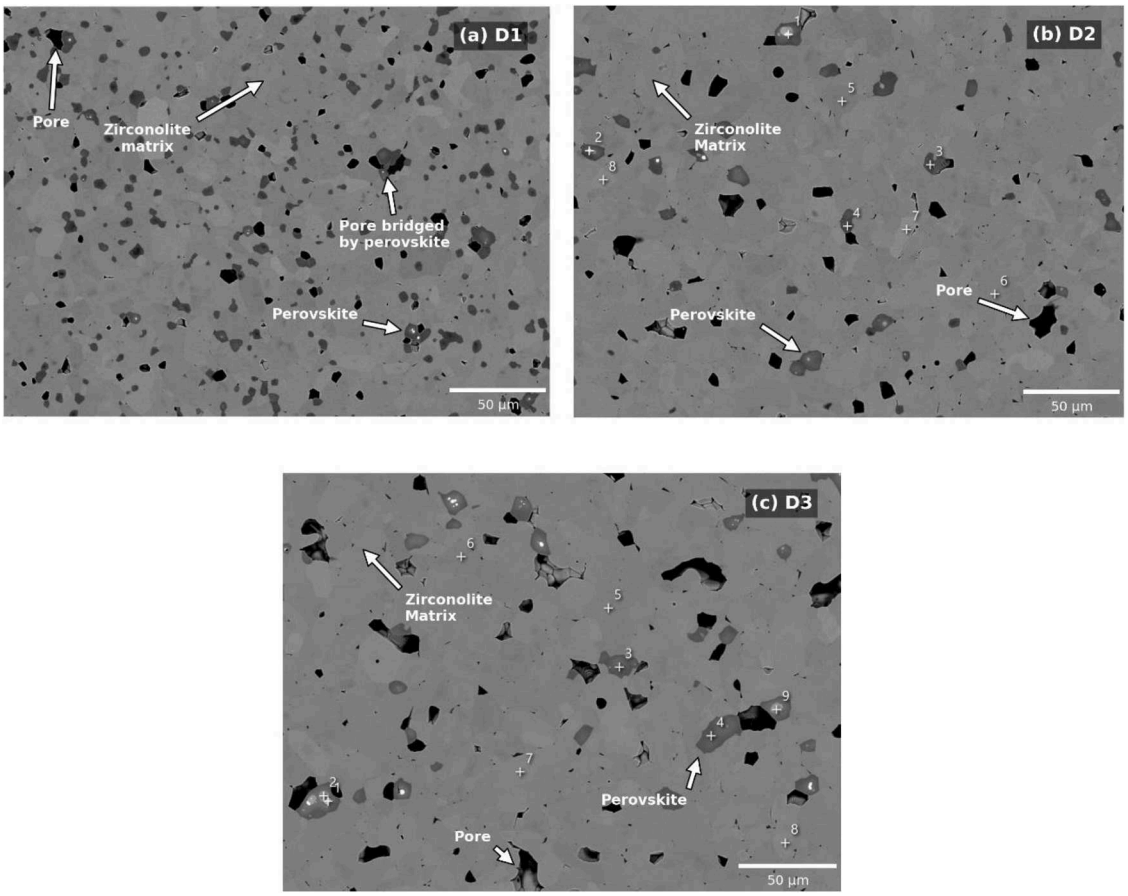


Fig. 11. SEM images of the D1, D2, and D3 sintered pellets in (a), (b), and (c), respectively.

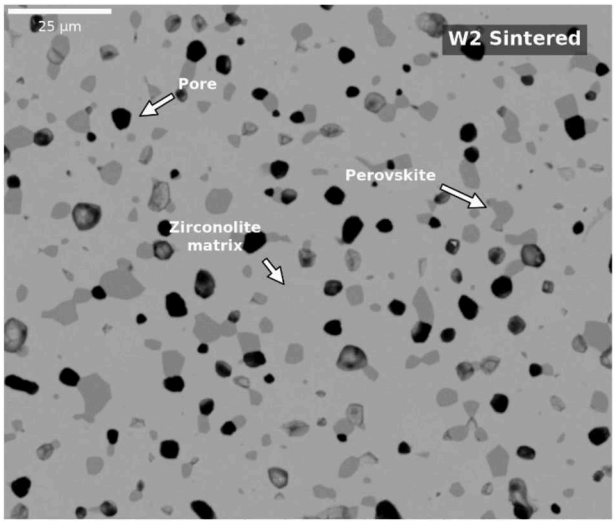


Fig. 12. SEM image of the W2 sintered pellet.

variation within the zirconolite, though inclusions consistent with perovskite were found to show some association with pores. These inclusions formed bridges between neighbouring voids in some cases, suggesting that secondary phase formation and pore evolution may have been coupled, though assessment of this was beyond the scope of this study.

4.4. *Elemental homogeneity*

To assess global elemental homogeneity, the sintered pellets were examined by EDS, with the BSE and individual element images for D1, D2, D3 and W2 given in Fig. 13, Fig. 14, Fig. 15, and Fig. 16, respectively.

The dry route approach was not expected to necessarily be more susceptible to heterogeneity, though the route may place a greater reliance on mechanical mixing and milling to achieve chemical uniformity due to the bulk crystal structure of the feedstock. In the dry-route powder, homogenisation may potentially proceed via solid-solid interactions rather than through molecular scale mixing, and it is possible to theorise that this will have been more the case with the wet route which was previously shown to have a more disordered structure (Fig. 8). The literature has previously suggested that spatial zoning (e.g., inhomogeneities, inclusions, chemical banding) in the wasteform, which could be affected by these mechanisms, may influence the long-term performance of the material by creating chemically distinct regions with different durability and radiation resistance [38,39], though it was not possible to directly assess this based on the data presented here.

In all three dry route samples, the major cation distributions (Ca, Zr, Ti, Ce, and where applicable Hf and Gd) appeared uniform at the µm length-scale with no evidence for significant segregation beyond Ce-perovskite areas. In D1, the elemental maps were found to be uniform, consistent with a simplified chemistry. Introduction of the buffer and neutron absorbers in D2 did not produce any detectable heterogeneity at the µm length-scale, suggesting that the co-milling protocol was potentially sufficient to form a relatively homogeneous microstructure. In D3, which differed from D1 and D2 in terms of its powders' co-milling method, there was no evidence for any discernible improvement (or deterioration) in elemental uniformity relative to D2 (or D1).

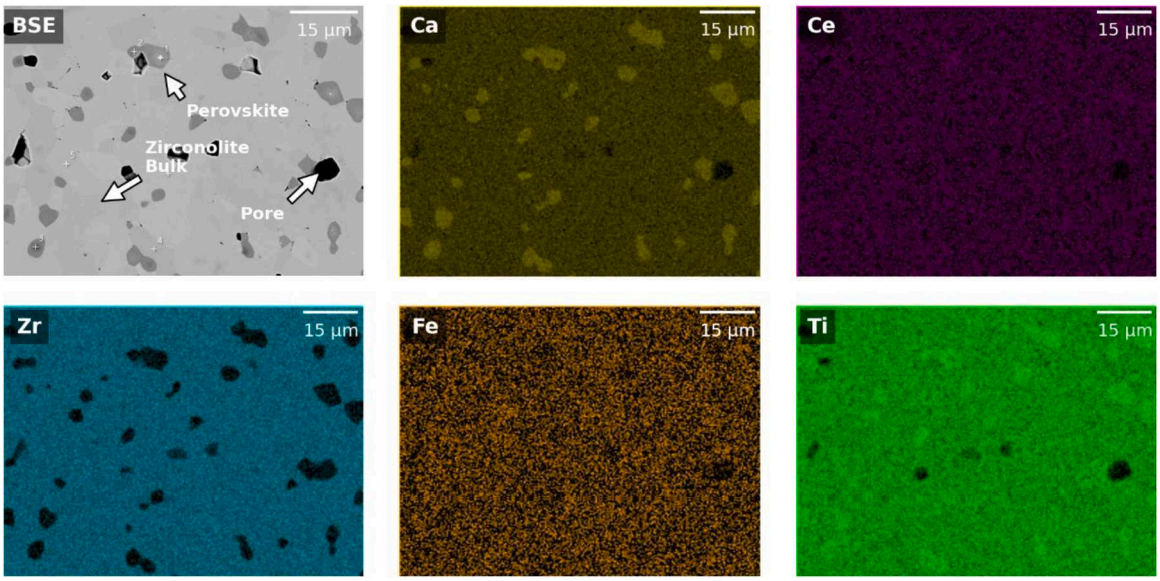


Fig. 13. Backscattered electron image of and elemental distributions in the D1 sintered pellet.

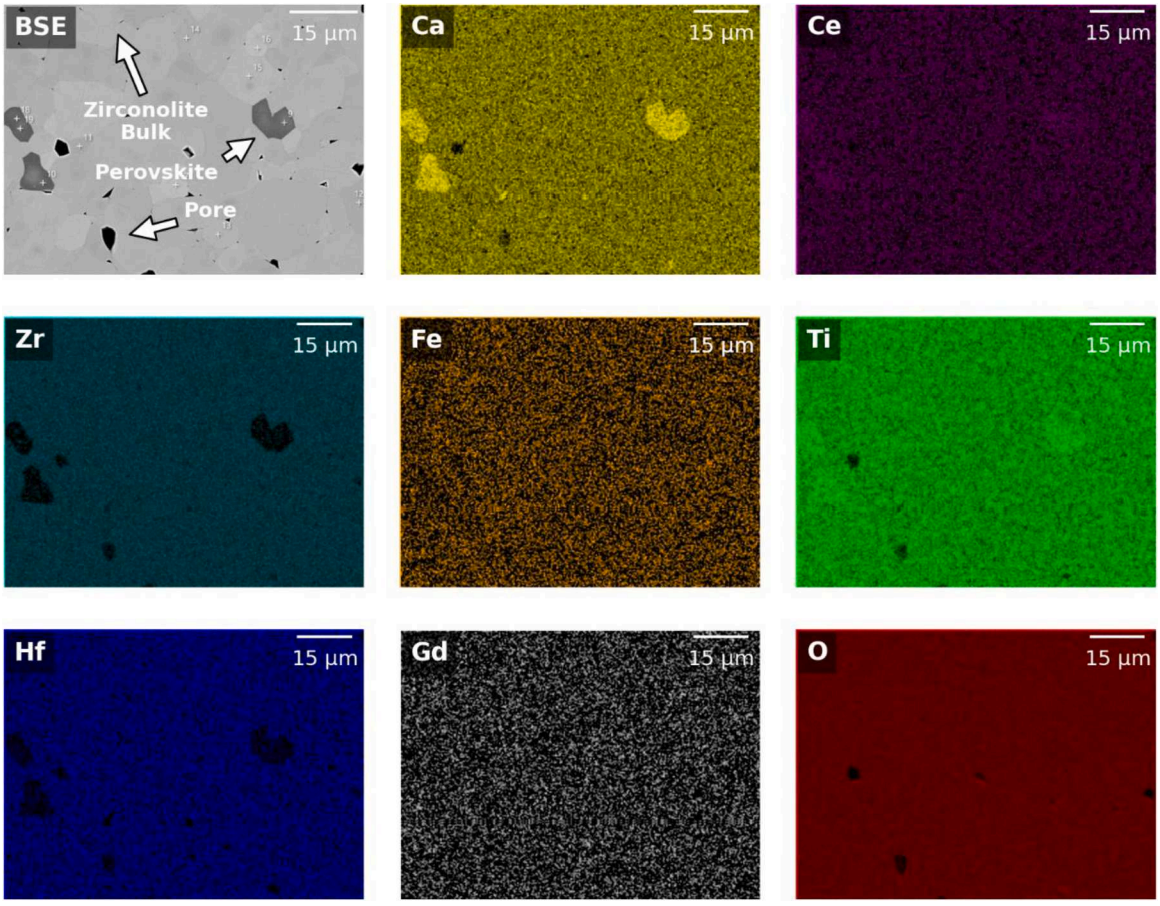


Fig. 14. Backscattered electron image of and elemental distributions in the D2 sintered pellet.

At the µm length-scale accessible to the SEM-EDS measurements, the wet-route pellet indicated continuous elemental distributions without evidence of any large-scale segregation, except for the perovskite regions which were identified. Despite the presence of porosity in the BSE data, no systematic enrichment or depletion of individual elements was clearly indicated around pore boundaries. This suggested that the wet route precursor chemistry and subsequent processing were effective in achieving bulk homogenisation at the length scale which could be reliably probed here, prior to consolidation of the material into a solidified pellet.

In the case of this assessment, SEM-EDS mapping cannot resolve zirconolite polytypes. The technique is also inherently limited in

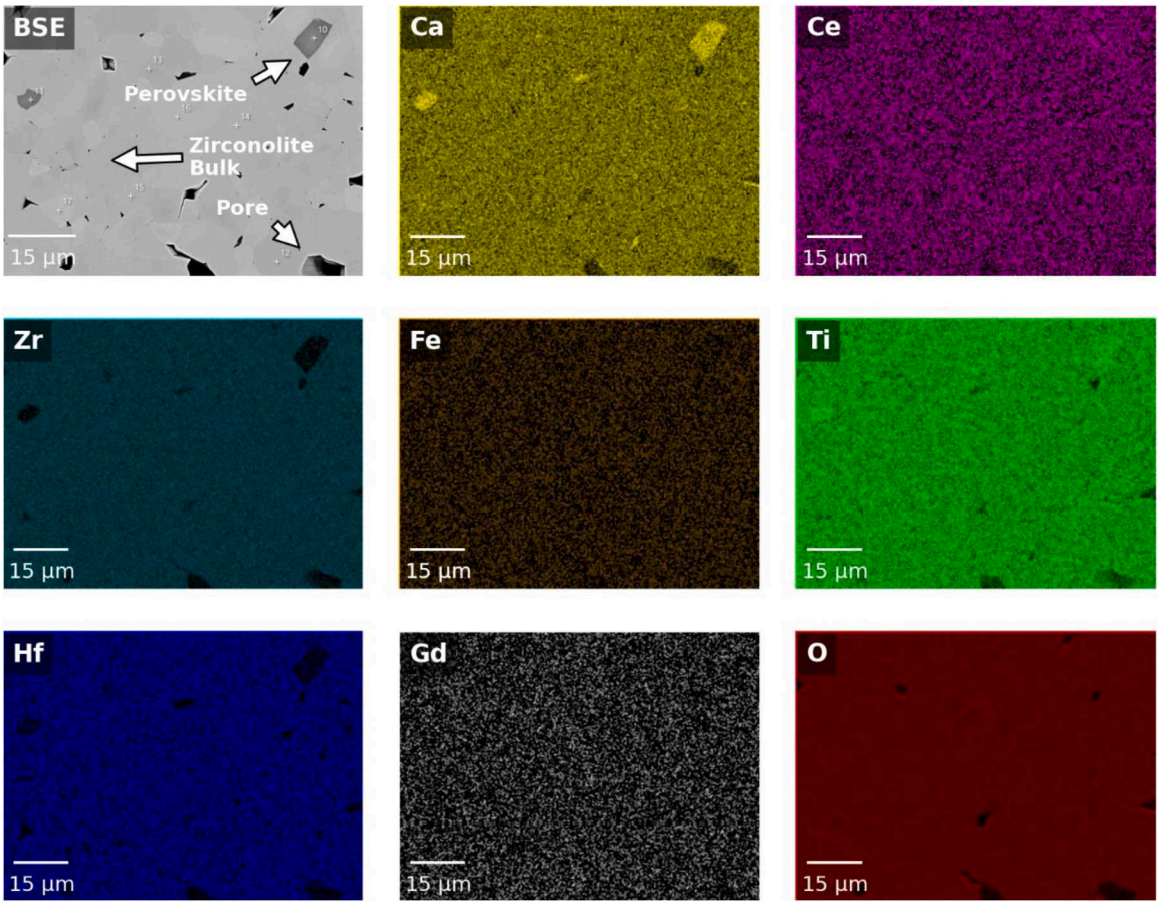


Fig. 15. Backscattered electron image of and elemental distributions in the D3 sintered pellet.

sensitivity to very small compositional variations, though it can provide a useful assessment of chemical uniformity at the µm length-scale used here. In all cases, the apparent homogeneity in these sintered pellets cannot rule out any effect which occurs on a length-scale to which the technique is insensitive, and a full assessment of these pellets ideally requires an instrument which is sensitive to the sample chemistry at a higher spatial resolution.

4.5. *Phase composition*

While SEM data can probe the spatial distribution and morphology of microstructural features and elements, it cannot evaluate short-range order in the structures present without supplementary methods. Therefore, X-ray diffraction profiles were collected. The D1, D2 and D3 XRD profiles are presented in Fig. 17.

In this case, all three examples were dominated by zirconolite phases, which coexisted alongside a secondary perovskite-type structure. A closely spaced pair of reflections was found in the ~30–31°2θ region, and this feature was tentatively assigned to overlapping contributions from the 2 M and 3T polytypes [40], with the lower angle component attributed to zirconolite-2 M and the higher angle to −3T. It was supposed that the asymmetric peak broadening observed at the base of this reflects interference between the two polytypes, rather than instrument peak broadening (which was not observed in any other peak).

Reflections which could be attributed to the 3T polytype (e.g., the split feature at 28.86°2θ and the low angle reflection at 15.84°2θ) were shown in D2 and D3, while being difficult to resolve in D1. Perovskite, which is a common accessory phase in synthetic zirconolites [41], was observed in all samples, with reflections at 23.37°2θ, the closely spaced doublet at 31.99°2θ /32.06°2θ, 32.94°2θ, and an additional feature at 47.70°2θ. It can therefore be proposed that, from the overall sharp Bragg peaks, absence of diffuse scattering beyond air scattering in the low-2θ range, and the well-defined fingerprint reflections, a highly crystalline structure was formed in all three dry route samples.

While the XRD pattern data confirmed the coexistence of zirconolite polytypes and minor secondary phases, these results alone could not accurately predict relative phase abundances. The data were therefore analysed by Rietveld refinement using the method provided to assess systematic differences in phase assemblage, with these presented in Fig. 18(a)-(d).

To account for the effective perovskite solid solution, this was modelled as two independent phases with closely matching compositions, one incorporating Ce and one without. For clarity in presentation, these were combined into a single perovskite-titanate, with the associated uncertainties propagated in quadrature to reflect their independent refinement errors.

The un-merged refined contributions were reported as 6.19 wt.% Ce-bearing perovskite (with the non-Ce-bearing phase undetected) in D1; 2.67 wt.% Ce-bearing and 0.45 wt.% non-Ce-bearing in D2; and 2.98 wt.% Ce-bearing and 0.26 wt.% non-Ce-bearing in D3. The minor fractions resolved for the non-Ce-bearing phase in D2 and D3 fall well below the typical 1–2 wt.% detection and quantification limits of laboratory XRD and can therefore only be interpreted as semi-quantitative indicators within the refinement constraints rather than definitive absolute values. Nevertheless, because the non-Ce-bearing perovskite remained undetected in D1 and only emerged as a negligible trace contributor in D2 and D3, the refinement strongly suggests a robust structural partitioning of the Ce plutonium-surrogate preferentially into the perovskite phase across all investigated samples.

An increase in 3T content was observed between D1 (no 3T present)

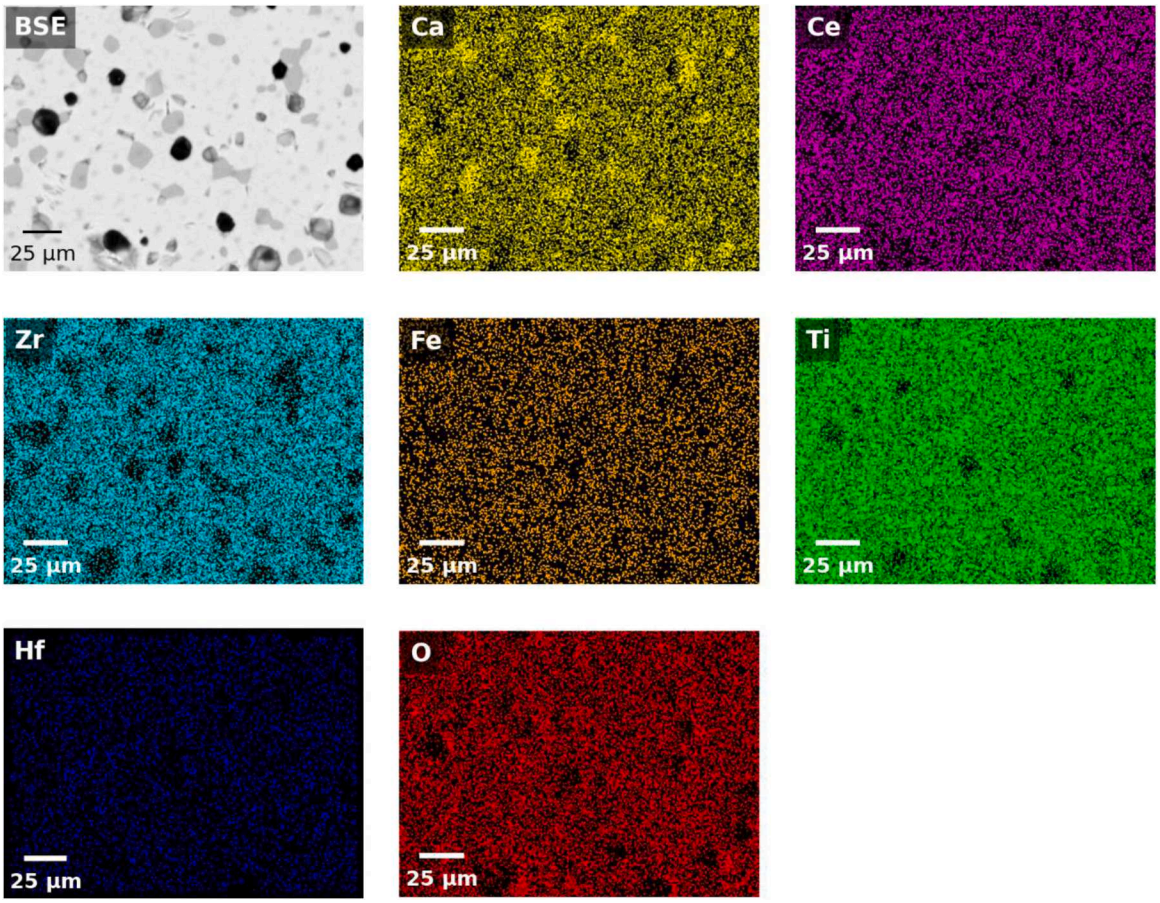


Fig. 16. Backscattered electron image of and elemental distributions in the W2 sintered pellet.

to D2/D3, with a concomitant decrease in the 2 M fraction; this demarcation of 2 M and 3T phases may reflect changes in cation distribution and short-range ordering introduced by the Ti/Hf buffer which changed how the zirconolite crystallised. Consistent with the earlier interpretation of the Ti-Hf buffer acting to moderate the availability of Ti and therefore suppress rapid pairing of Ca-Ti into perovskite, the reduced perovskite-titanate content in the D2 and D3 samples, compared to D1, is unsurprising and suggests that a greater fraction of the available Ca-Ti-Zr was retained within the zirconolite. The corresponding occurrence of the zirconolite-3T fraction in D2 and D3 may therefore reflect how this additional material was accommodated with small changes in arrangement causing formation of the 3T structure to be favoured.

The phase assemblage of the wet route W2 pellet was also evaluated: the XRD profile is shown in Fig. 19, with the phase composition values in Fig. 20. Refinement of the diffraction data yielded phase fractions of 49.8(32) wt.% zirconolite-2 M, 37.5(25) wt.% zirconolite-3T, and 12.7 (9) wt.% perovskite modelled as a single solid solution endmember; no tertiary accessory phases were identified at this point. These results demonstrate that W2 formed a zirconolite-rich ceramic comprised of both −2 M and −3T polytypes, together with a perovskite secondary phase.

The perovskite content identified in the W2 phase assemblage may reflect the kinetics of phase evolution from the wet-route precursor. The high specific surface area of the precursor, alongside the substantial changes to the microstructure which occur during heating (e.g., rapid degassing), may have enhanced local redistribution of the constituent species. This could have generated transient Ca-rich regions in which Ca-Ti reaction and perovskite nucleation were locally favoured, causing this phase to form preferentially. The measurements presented here, however, are not capable of directly resolving the evolution of the phase composition during sintering of the ceramic, and so this interpretation remains tentative without access to instrumentation capable of being able to carry this out.

5. Discussion

This work has examined both wet and dry processing routes for a single zirconolite-rich precursor, followed by co-milling with CeO_2 (as a surrogate of PuO_2), and then production of a densified ceramic using a CPS approach. Both approaches have demonstrated the potential to produce relatively high sintered density pellets, predominant in zirconolite (2M/3T phases) and with a good degree of chemical homogeneity at the micron scale, notwithstanding the perovskite 'inclusion' regions apparent in all pellet samples.

Regarding the zirconolite-rich precursor powders, analysis of PSD and SEM data demonstrated that the wet and dry synthesis routes generated zirconolites with different formation mechanisms. Fracture-dominated fragments likely arising from pulverisation of previously sintered pellets were identified in the dry route, whereas agglomerated structures were apparent in the wet. Albeit with only a limited rheometry investigation carried out, the wet and dry powders had differing responses to confined flow.

In nuclear facility powder handling systems (e.g., gloveboxes, shielded hoppers, transfer lines), powders are unlikely to be regularly subject to high shear but, rather, more likely to experience localised, relatively low-shear mobilisation to reduce risks from dust generation, criticality, and contamination spread (e.g., gravity feeding, perhaps with fluidisation if needed [42]). Agglomerated systems such as the wet route powder materials might be more prone to intermittent discharge,

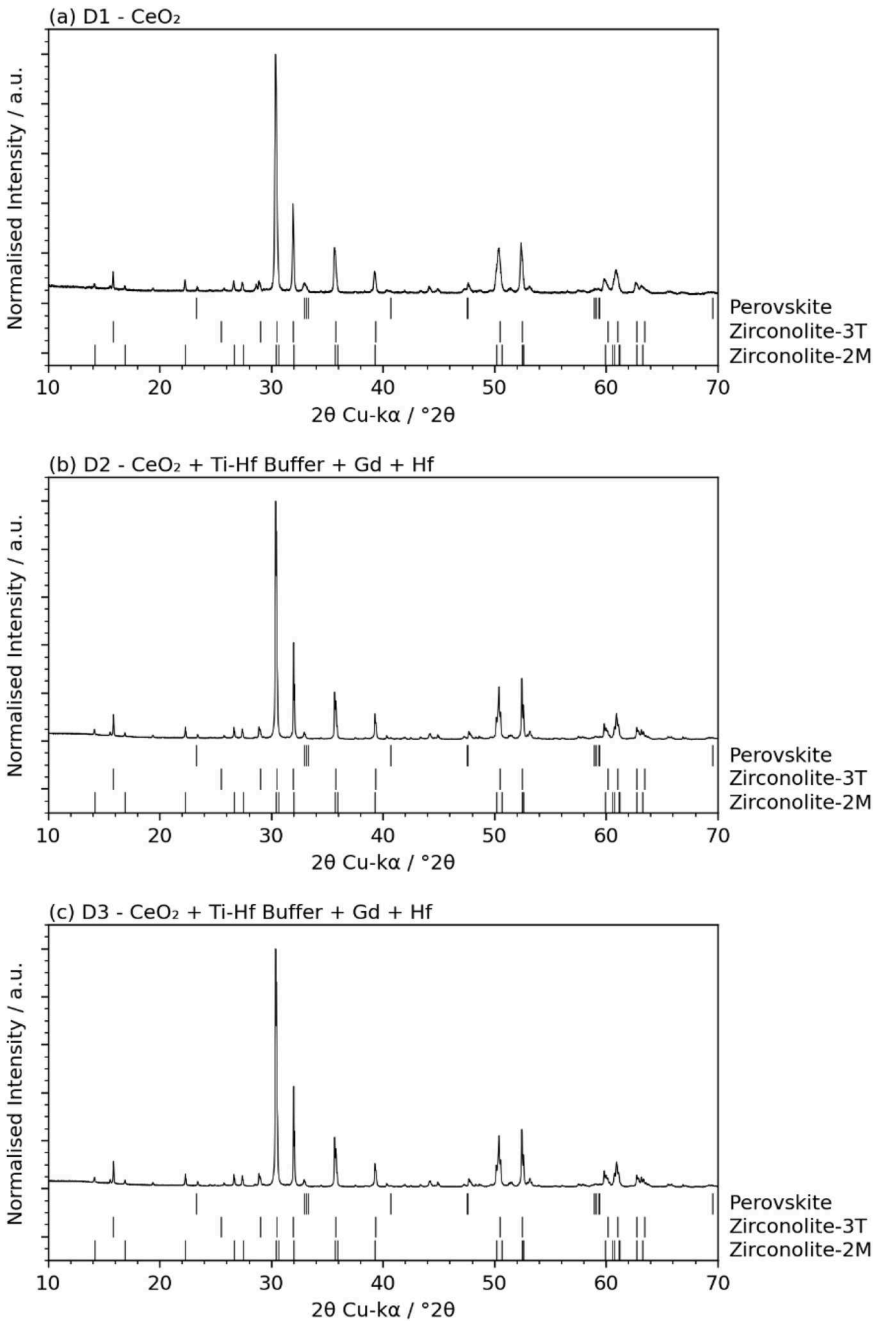


Fig. 17. XRD profiles for samples D1 in (a), D2 in (b) and D3 in (c), with the characteristic peak positions of perovskite, zirconolite-2 M and zirconolite-3T also shown.

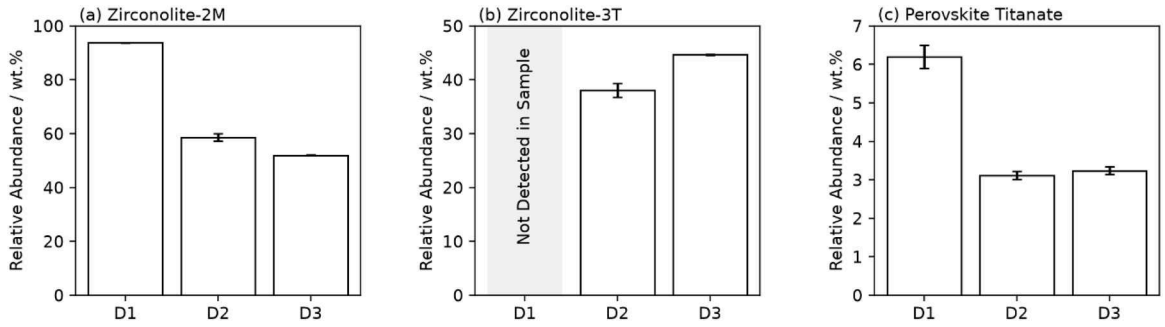


Fig. 18. The phase assemblage of pellet samples D1, D2, and D3.

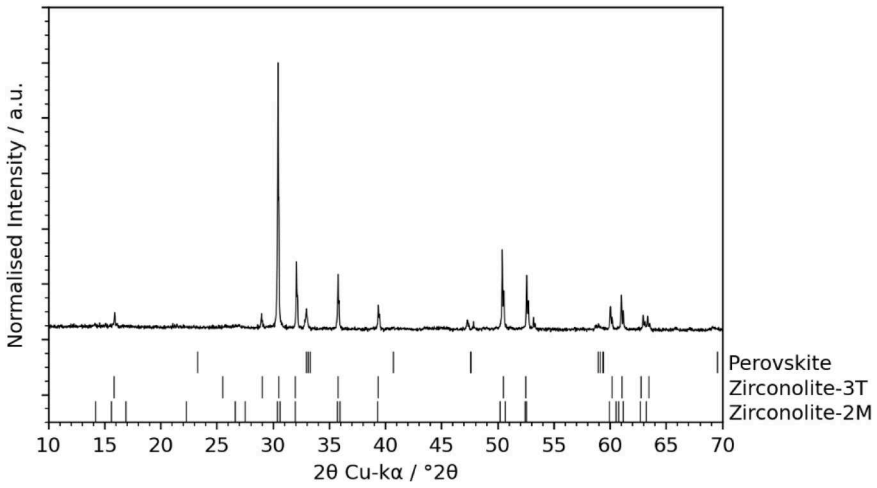


Fig. 19. XRD profile for W2 sintered pellet, with the characteristic peak positions of perovskite, zirconolite-2 M and zirconolite-3T also shown.

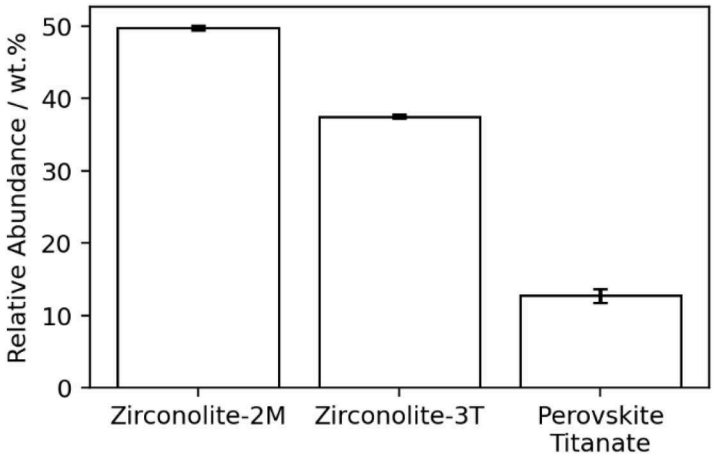


Fig. 20. Phase assemblage of the W2 pellet.

arching, and ratholing [43]; this might become problematic in a plutonium-active environment, where manual intervention is generally more difficult (or perhaps not possible) and unplanned process stoppages or surges can compromise containment, accuracy, and safety.

Thermogravimetric analysis indicated that the wet route powder contained a significant decomposable fraction prior to formation of the zirconolite, while the dry route material was relatively stable throughout, with the as-produced D1 powder having < 1 wt.% loss up to 1000 °C. As discussed previously, the measurements were acquired with differing sample masses and are not interpreted here as comparable profiles. These therefore provide independent indications of the extent of mass loss occurring in each material. For W1 the substantial mass loss demonstrates an appreciable content of decomposable material remained prior to formation of the final ceramic, although chemical identification of the evolved species was not performed here. If such material were retained into a subsequent sealed consolidation stage (e.g., HIP), gas evolution during heating could potentially influence densification or cause defect formation. This would need to be considered when defining thermal conditioning or degassing requirements for a future process such as HIP, which was not investigated here.

Following CPS, SEM and EDS showed that both routes could produce pellets with a high degree of uniformity at the μm length-scales to which the technique is sensitive. In the dry route, no large-scale elemental separation was evident within the mapped areas, beyond the formation of perovskite. Similarly, the W2 pellet showed no evidence of large-scale elemental separation at the accessible length-scale, though this cannot be excluded at shorter length-scales; these observations are able to support micron-scale chemical uniformity following thermal treatment but are unable to account for complete compositional homogeneity at all length scales.

XRD and Rietveld refinement provided some detail about the phase assemblages within the independently analysed pellet datasets. Perovskite was consistently identified as a secondary phase in all samples. Within the internally consistent dry-route dataset, a lower perovskite abundance was reported by refinement in D2 and D3, relative to D1. This suggests that the presence of the Ti-Hf buffer influenced the formation of secondary phases, though XRD cannot describe the mechanism which is responsible for this effect. Refinement of the W2 pellet also suggested the presence of perovskite, though the W2 diffraction data were collected using a different diffractometer and so it is not possible to quantitatively compare the refined abundance of this phase with the dry-route samples. The presence of perovskite within the W2 pellet may reflect kinetic effects during decomposition and crystallisation of the wet-route precursor, although the methods applied in this study were not able to resolve the precise nature of the mechanism responsible for this.

With a lookahead to future possible scale-up (i.e., 'industrialisation') of a single zirconolite-rich precursor approach in a plutonium-active context, a key issue is to acknowledge that powder behaviour evolves depending on processing conditions and cannot be simplistically treated as some 'fixed' property. Each stage through formation of the zirconolite-rich precursor, and subsequent co-milling with CeO_2 and

production of a near fully dense zirconolite-based ceramic, might have knock-on implications for powder stability, segregation risk, packing behaviour, and containment. In a nuclear environment, manual intervention is limited and failure modes should ideally be engineered out rather than managed via subsequent human intervention. Therefore, this work highlights that process selection must be informed not only by zirconolite phase assemblage and stoichiometry, but also by how precursor powders behave under the confined, low-shear, and deployment-defined handling conditions. By linking synthesis history, thermal stability, and confined flow, to specific steps in the zirconolite fabrication process, this study provides a framework for designing zirconolite-based wasteforms which are not only chemically suitable, but also operationally robust and controllable when deployed at industrial scale.

6. Conclusions

Both solid-state ('dry') and liquid chemical ('wet') based powder synthesis routes have been found to be able to result in zirconolite-based ceramics (sintered pellets) which are likely to be suitable for Pu immobilisation: high sintered density (> 90 % TD), good bulk chemical homogeneity and well-defined phase assemblages have been observed.

Based on the evidence presented by characterisation of the D1 powder, the dry route formed a zirconolite-rich powder with a low SSA, alongside improved powder handling characteristics, and a flow behaviour which was more predictable. The data resulting from characterisation of the W1 powder indicated that the wet route produced a fine and reactive material. XRD demonstrated that both routes produced well-defined zirconolite-rich materials which contained perovskite as a secondary phase. Within the dry-route dataset, incorporation of the Ti/Hf buffer could be associated with reduced perovskite formation in D2 and D3 relative to D1. The independently refined W2 dataset demonstrated a zirconolite-rich 2M/3T assemblage which also coexisted alongside perovskite. Moreover, although indeed 'wet' in terms of most of its starting chemicals, the wet route approach (in the way delivered in the present work) still involves a significant amount of 'dry' processing, including calcination and milling of the calcined powder.

The data presented here suggested that the method used to produce the single zirconolite-rich precursor can influence its powder characteristics and the associated requirements of processing. Under the consistent conditions investigated, the dry-route precursor reported a more predictable flow behaviour, whereas the wet-route material showed finer particle characteristics and higher specific surface area. The wet route powder also reported a significant mass loss on heating, under the analytical conditions used to assess the W2 sample. These observations suggest that it is important to consider powder handling and pre-treatment alongside the subsequent wasteform formation when developing a single-precursor process.

As such, it is recommended that future work, rather than consider processing aspects as an 'afterthought' relative to the wasteform characteristics, should adopt an integrated methodology linking synthesis route, conditioning, and consolidation, to handling and containment requirements. Process-related aspects that could be investigated include the chemistry of synthesis (e.g., different wet chemistries), mechanisms of particle formation and agglomeration (e.g., different approaches to size reduction), and removal of volatile species by intermediate thermal conditioning. Integrating these with control of the phase assemblage (including suppression of secondary phase formation) could support the development of zirconolite wasteform routes which are robust by design, compatible with remote deployment, and industrially scalable.

CRediT authorship contribution statement

James E Vigor: Writing – original draft, Validation, Methodology, Formal analysis. **Aidan A Friskney:** Visualization, Validation, Methodology, Investigation, Formal analysis. **Reuben R Gilbert:** Writing – review & editing, Investigation, Conceptualization. **Lewis R Blackburn:** Writing – review & editing, Supervision, Resources, Conceptualization. **Katie Hadley:** Resources, Investigation, Data curation. **Paul Gilchrist:** Supervision, Project administration, Conceptualization. **Richard White:** Software, Resources, Investigation, Formal analysis, Data curation. **Jason Farrell:** Writing – review & editing, Resources, Project administration, Methodology, Investigation, Funding acquisition, Formal analysis, Conceptualization.

Declaration of competing interest

The authors declare that they have no known competing financial interests or personal relationships that could have appeared to influence the work reported in this paper.

Acknowledgements

We are grateful for comments from Paul Cook and Chris Gallagher (both of the Nuclear Decommissioning Authority). Lewis Blackburn gratefully acknowledges funding from the Royal Academy of Engineering through the Research Fellowship Scheme.

Data availability

The datasets generated during and/or analysed during the study are not available due to restrictions related to the sensitive nature of the source materials.

References

[1] L.R. Blackburn, D.J. Bailey, S.K. Sun, L.J. Gardner, M.C. Stennett, C.L. Corkhill, N. C. Hyatt, Review of zirconolite crystal chemistry and aqueous durability, Adv. Appl. Ceram. 120 (2021) 69–83, https://doi.org/10.1080/17436753.2021.1877596.

[2] Q. Ai, S.K. Sun, Y. Tian, W.D. Xiao, Y. Zhao, S.H. Tan, W.M. Guo, H.T. Lin, Synthesis and leaching evaluation of entropy-stabilized zirconolite $Ca(Zr,Hf,Sn)_xTi_{3-x}O_7$ (x = 0.8–2.2), Chem. Eng. J. 527 (2026) 171972, https://doi.org/10.1016/j.cej.2025.171972.

[3] F. Jorion, X. Deschanels, T. Advocat, F. Desmouliere, J.N. Cachia, S. Peuget, D. Roudil, G. Leturcq, Zirconolite for minor actinide containment and alpha irradiation resistance, Nucl. Sci. Eng. 153 (2006) 262–271, https://doi.org/10.13182/NSE06-A2612.

[4] G. Deissmann, S. Neumeier, G. Modolo, D. Bosbach, Durability of potential plutonium wasteforms under repository conditions, Mineral. Mag. 76 (2012) 2911–2918, https://doi.org/10.1180/minmag.2012.076.8.06.

[5] A.J. Mason, A.A. Friskney, L.T. Haigh, M. Myszczynski, I. Aldean, A.B. Harvey-Reid, M.C. Stennett, L.R. Blackburn, Structural and thermal effects of Hf^{4+} substitution in $CaZr_{1-x}Hf_xTi_2O_7$ zirconolite, Ceram. Int. 51 (2025) 52074–52080, https://doi.org/10.1016/j.ceramint.2025.08.415.

[6] K. Zhang, D. Yin, Z. He, J. Xue, W. Zhao, H. Zhang, Combustion synthesis and characterizations of Sm_2O_3-doped zirconolite-rich waste forms with CuO as oxidant, J. Rare Earths 37 (2019) 1359–1365, https://doi.org/10.1016/j.jre.2018.11.020.

[7] S. McCaugherty, A.P. Grosvenor, Low-temperature synthesis of $CaZrTi_2O_7$ zirconolite-type materials using ceramic, coprecipitation, and sol–gel methods, J. Mater. Chem. C 7 (2019) 177–187, https://doi.org/10.1039/C8TC04560G.

[8] S.V. Yudintsev, M.S. Nickolsky, M.I. Ojovan, O.I. Stefanovsky, V.I. Malkovsky, A. S. Ulanova, L.R. Blackburn, Zirconolite matrices for the immobilization of REE–actinide wastes, Ceramics 6 (3) (2023) 1573–1622.

[9] H.M. Rietveld, A profile refinement method for nuclear and magnetic structures, Acta Crystallogr 2 (1969) 65–71, https://doi.org/10.1107/S0021889869006558.

[10] H.J. Rossell, Zirconolite - a fluorite-related superstructure, Nature 283 (1980) 282–283, https://doi.org/10.1038/283282a0.

[11] I.E. Grey, W.G. Mumme, T.J. Ness, R.S. Roth, K.L. Smith, Structural relations between weberite and zirconolite polytypes—refinements of doped 3T and 4M $Ca_2Ta_2O_7$ and 3T $CaZrTi_2O_7$, J. Solid State Chem. 174 (2003) 285–295, https://doi.org/10.1016/S0022-4596(03)00222-6.

[12] A. Beran, E. Libowitzky, T. Armbruster, A single-crystal infrared spectroscopic and X-ray-diffraction study of untwinned San Benito perovskite containing OH groups, Can. Mineral. 34 (1996) 803–809. https://pubs.geoscienceworld.org/mac/canmin/article-pdf/34/4/803/3446767/803.pdf.

[13] M. Okrusch, R. Hock, U. Schüssler, A. Brummer, M. Baier, H. Theisinger, Intergrown niobian rutile phases with Sc- and W-rich ferrocolumbite: an electron-microprobe and rietveld study, Am. Mineral. 88 (2003) 986–995, https://doi.org/10.2138/am-2003-0706.

[14] T.E. Weirich, M. Winterer, S. Seifried, H. Hahn, H. Fuess, Rietveld analysis of electron powder diffraction data from nanocrystalline anatase, TiO_2,

Ultramicroscopy 81 (2000) 263–270, https://doi.org/10.1016/S0304-3991(99)00189-8.
[15] L. Pauling VII, The crystal structure of pseudobrookite, Z. Kristallogr. 73 (1930) 97–112, https://doi.org/10.1524/zkri.1930.73.1.97.
[16] K. Zhang, D. Yin, K. Xu, H. Zhang, Self-propagating synthesis and characterization studies of Gd-bearing Hf-zirconolite ceramic waste forms, Materials (Basel) 12 (2019) 178, https://doi.org/10.3390/ma12010178.
[17] B.M. Patil, G.C. Wadhawa, A.C. Chaskar, P.S. Walke, Low-temperature synthesis and thermal expansion of nanocrystalline monoclinic zirconolite ceramics, J. Therm. Anal. Calorim. 148 (2023) 7591–7596, https://doi.org/10.1007/s10973-023-12269-z.
[18] A.A. Friskney, I. Aldean, C.L. Corkhill, L.R. Blackburn, Process development of zirconolite ceramics for Pu disposition: use of a CuO sintering aid, Ceramics 6 (2023) 678–685, https://doi.org/10.3390/ceramics6010041.
[19] S. Kondo, A. Ishihara, E. Tochigi, N. Shibata, Y. Ikuhara, Direct observation of atomic-scale fracture path within ceramic grain boundary core, Nat. Commun. 10 (2019) 2112, https://doi.org/10.1038/s41467-019-10183-3.
[20] S.-J.L Kang, J.G. Fisher, Grain growth in polycrystalline materials: current understanding and future research directions, Open Ceramics 16 (2023) 100484, https://doi.org/10.1016/j.oceram.2023.100484.
[21] C. Tian, Effects of structural factors of hydrated TiO_2 on rutile TiO_2 pigment preparation via short sulfate process, Sci. Rep. 10 (2020) 7999, https://doi.org/10.1038/s41598-020-64976-4.
[22] J. Wang, J. Li, Y. Li, L. Li, X. Su, H. Li, Y. Hu, X. Xu, Flash viscous flow sintering of nanostructured amorphous ZrO_2–Y_2O_2 composite ceramics starting from a partially amorphous precursor powder, Ceram. Int. 50 (2024) 28926–28936, https://doi.org/10.1016/j.ceramint.2024.05.204.
[23] K.S.P. Karunadasa, C.H. Manoratne, Microstructural view of anatase to rutile phase transformation examined by in-situ high-temperature X-ray powder diffraction, J. Solid State Chem. 314 (2022) 123377, https://doi.org/10.1016/j.jssc.2022.123377.
[24] C. Perrino, E. Marconi, L. Tofful, C. Farao, S. Materazzi, S. Canepari, Thermal stability of inorganic and organic compounds in atmospheric particulate matter, Atmos. Environ. 54 (2012) 36–43, https://doi.org/10.1016/j.atmosenv.2012.02.078.
[25] G. Lo Dico, L. Lisuzzo, V. Carcelén, G. Cavallaro, M. Haranczyk, Thermogravimetric analysis of moisture in natural and thermally treated clay materials, Materials (Basel) 17 (2024) 2231, https://doi.org/10.3390/ma17102231.
[26] Y. Garanin, R. Shakirzyanov, D. Borgekov, A. Kozlovskiy, N. Volodina, D. Shlimas, M. Zdorovets, Study of morphology, phase composition, optical properties, and thermal stability of hydrothermal zirconium dioxide synthesized at low temperatures, Sci. Rep. 14 (2024) 29398, https://doi.org/10.1038/s41598-024-80399-x.
[27] S.J. Kemp, A.L. Lewis, J.C. Rushton, Detection and quantification of low levels of carbonate mineral species using thermogravimetric-mass spectrometry to validate CO_2 drawdown via enhanced rock weathering, Appl. Geochem. 146 (2022) 105465, https://doi.org/10.1016/j.apgeochem.2022.105465.
[28] A. Zhao, B. Xiong, Y. Han, H. Tong, Thermal decomposition paths of calcium nitrate tetrahydrate and calcium nitrite, Thermochim. Acta 714 (2022) 179264, https://doi.org/10.1016/j.tca.2022.179264.
[29] R. Hofman, J.G.F. Westheim, V.A.C. Haanappel, T. Fransen, P.J. Gellings, The pyrolytic decomposition of metal alkoxides (di-acetoxy-di-t-butoxy-silane, DADBS) during chemical vapour deposition of thin oxide films, Thermochim. Acta 215 (1993) 329–335, https://doi.org/10.1016/0040-6031(93)80109-N.
[30] A. Zhao, B. Xiong, Y. Han, H. Tong, Thermal decomposition paths of calcium nitrate tetrahydrate and calcium nitrite, Thermochim. Acta 714 (2022) 179264, https://doi.org/10.1016/j.tca.2022.179264.
[31] D. Sergeev, B.H. Reis, M. Ziegner, I. Roslyakova, M. to Baben, K. Hack, M. Müller, Comprehensive analysis of thermodynamic properties of calcium nitrate, J. Chem. Thermodyn. 714 (2022) 179264, https://doi.org/10.1016/j.tca.2022.179264.
[32] L.R. Blackburn, L.J. Gardner, S.K. Sun, E.R. Maddrell, M.C. Stennett, C.L. Corkhill, N.C. Hyatt, Hot isostatically pressed zirconolite wasteforms for actinide immobilisation, IOP Conf. Ser.: Mater. Sci. Eng. 818 (2020) 012010, https://doi.org/10.1088/1757-899X/818/1/012010.
[33] D.J. Bailey, S.M. Lawson, S.K. Sun, M.C. Stennett, T.H. Lee, B. Ravel, C.L. Corkhill, J. Heo, N.C. Hyatt, A new approach to the immobilisation of technetium and transuranics: Co-disposal in a zirconolite ceramic matrix, J. Nucl. Mater. 528 (2020) 151885, https://doi.org/10.1016/j.jnucmat.2019.151885.
[34] K.G. Webber, O. Clemens, V. Buscaglia, B. Malič, R.K. Bordia, T. Fey, U. Eckstein, Review of the opportunities and limitations for powder-based high-throughput solid-state processing of advanced functional ceramics, J. Eur. Ceram. Soc. 44 (2024) 116780, https://doi.org/10.1016/j.jeurceramsoc.2024.116780.
[35] Z.J. Wei, W. Bao, S.K. Sun, L.R. Blackburn, S.H. Tan, L.J. Gardner, W.M. Guo, F. Xu, N.C. Hyatt, H.T. Lin, Synthesis of zirconolite-2M ceramics for immobilisation of neptunium, Ceram. Int. 47 (2021) 1047–1052, https://doi.org/10.1016/j.ceramint.2020.08.220.
[36] L.R. Blackburn, S.K. Sun, S.M. Lawson, L.J. Gardner, H. Ding, C.L. Corkhill, E. R. Maddrell, M.C. Stennett, N.C. Hyatt, Synthesis and characterisation of Ca1-xCexZrTi2-2xCr2xO7: analogue zirconolite wasteform for the immobilisation of stockpiled UK plutonium, J. Eur. Ceram. Soc. 40 (2020) 5909–5919, https://doi.org/10.1016/j.jeurceramsoc.2020.05.066.
[37] L.R. Blackburn, S.K. Sun, L.J. Gardner, M.C. Stennett, C.L. Corkhill, N.C. Hyatt, A systematic investigation of the phase assemblage and microstructure of the zirconolite $CaZr_{1-x}Ce_xTi_2O_7$ system, J. Nucl. Mater. 535 (2020) 152137, https://doi.org/10.1016/j.jnucmat.2020.152137.
[38] M.B. Kachalov, M.I. Ozhovan, P.P. Poluéktov, Role of inhomogeneities in the fracturing of matrices with radioactive waste, Sov. At. Energy 63 (1988). https://www.osti.gov/biblio/6423255.
[39] M.I. Ojovan, B.E. Burakov, W.E. Lee, Radiation-induced microcrystal shape change as a mechanism of wasteform degradation, J. Nucl. Mater. 501 (2018) 162–171, https://doi.org/10.1016/j.jnucmat.2018.01.030.
[40] I.E. Grey, et al., Structural relations between weberite and zirconolite polytypes—refinements of doped 3T and 4M $Ca_2Ta_2O_7$ and 3T $CaZrTi_2O_7$, J. Solid-State Chem. 174 (2) (2003) 285–295.
[41] I. Aldean, S.K. Sun, M.C.D. Wilkins, L.J. Gardner, A.R. Mason, M.C. Stennett, C. L. Corkhill, N.C. Hyatt, L.R. Blackburn, Synthesis and characterisation of Ce-doped zirconolite $Ca_{0.80}Ce_{0.20}ZrTi_{1.60}M_{0.40}O_7$ (M= Fe, Al) formed by reactive spark plasma sintering (RSPS), MRS Adv. 7 (2022) 75–80, https://doi.org/10.1557/s43580-022-00221-6.
[42] J.R. Frederickson, R.C. Eschenbaum, L.H. Goldmann, Powder handling for automated fuel processing, HEDL-SA–3690. https://inis.iaea.org/records/12wkg-17177, 1989.
[43] J.M. Valverde, A. Castellanos, Effect of compaction history on the fluidization behavior of fine cohesive powders, Phys. Rev. E 73 (2006) 056310, https://doi.org/10.1103/PhysRevE.73.056310.